Cell Biomaterials

Article

Variations in mineral prestrain, nanostructure, and microarchitecture play a role in intervertebral disc loading

Graphical abstract

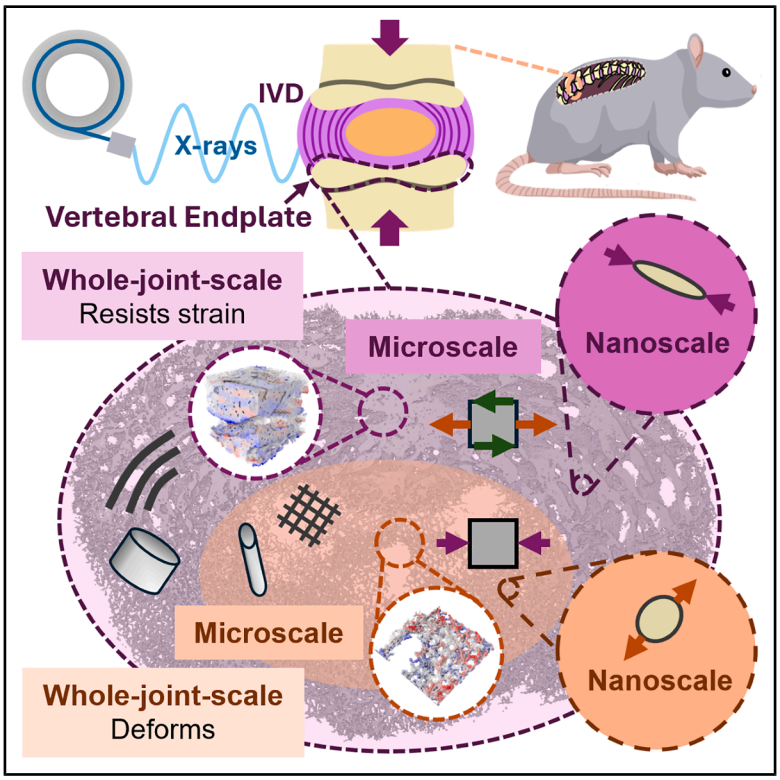

Highlights

- Multimodal synchrotron imaging reveals nano-to-microscale structure and strain
- Structural adaptation of mineralized tissues linked to local mechanical environment
- Nanoscale mineral prestrain contributes to joint-level mechanical behavior
- Regional endplate variation linked to the mechanical function of the disc

Authors

Alissa L. Parmenter, Elis Newham, Aikta Sharma, ..., Andrew A. Pitsillides, Himadri S. Gupta, Peter D. Lee

Correspondence

alissa.parmenter.20@ucl.ac.uk (A.L.P.), peter.lee@ucl.ac.uk (P.D.L.)

In brief

This study leverages multiscale X-ray imaging to reveal the local mechanical environment in the vertebral endplates and how their microarchitecture, mineral crystallite structure, and intrinsic prestrain mediate load transfer between intervertebral discs and vertebral bones in the spine. Compared with calcified cartilage, bony regions exhibited higher tensile and shear strains, narrower mineral crystallites, and greater compressive prestrain. These insights into structure-function relationships across scales offer valuable guidance for the design of biomimetic materials and next-generation orthopedic implants.

Parmenter et al., 2025, Cell Biomaterials *1*, 100151
September 23, 2025
https://doi.org/10.1016/j.celbio.2025.100151

CellPress

Please cite this article in press as: Parmenter et al., Variations in mineral prestrain, nanostructure, and microarchitecture play a role in intervertebral disc loading, Cell Biomaterials (2025), https://doi.org/10.1016/j.celbio.2025.100151

Cell Biomaterials

CellPress
OPEN ACCESS

Article

Variations in mineral prestrain, nanostructure, and microarchitecture play a role in intervertebral disc loading

Alissa L. Parmenter,[1,2,3,10,*] Elis Newham,[4] Aikta Sharma,[1,5] Catherine M. Disney,[1,6] Hans Deyhle,[7,8] Federico Bosi,[1] Nick J. Terrill,[7] Brian K. Bay,[9] Andrew A. Pitsillides,[5] Himadri S. Gupta,[4] and Peter D. Lee[1,3,*]

[1]UCL Mechanical Engineering, Roberts Engineering Building, University College London, Torrington Place, London WC1E 7JE, UK
[2]UCL Medical Physics and Bioengineering, Malet Place Engineering Building, University College London, Gower Street, London WC1E 6BT, UK
[3]Research Complex at Harwell, Rutherford Appleton Laboratory, Harwell Oxford, Didcot OX11 0FA, UK
[4]School of Engineering and Materials Science, Queen Mary University of London, Mile End Rd, Bethnal Green, London E1 4NS, UK
[5]Comparative Biomedical Sciences, Royal Veterinary College, Royal College Street, London NW1 0TU, UK
[6]Division of Cell Matrix Biology & Regenerative Medicine, School of Biological Sciences, Faculty of Biology, Medicine and Health, Manchester M13 9PT, UK
[7]Diamond Light Source, Diamond House, Harwell Science and Innovation Campus, Fermi Ave, Didcot OX11 0DE, UK
[8]Biomaterials Science Center, Department of Biomedical Engineering, University of Basel, Hegenheimermattweg 167B/C, 4123 Allschwil, Switzerland
[9]School of Mechanical, Industrial, and Manufacturing Engineering, Oregon State University, 204 Rogers Hall 2000 SW, Monroe Avenue, Corvallis, OR 97331-6001, USA
[10]Lead contact
*Correspondence: alissa.parmenter.20@ucl.ac.uk (A.L.P.), peter.lee@ucl.ac.uk (P.D.L.)
https://doi.org/10.1016/j.celbio.2025.100151

THE BIGGER PICTURE Back pain is the leading cause of years lived with disability worldwide, often driven by degeneration of intervertebral discs (IVDs) and their interfaces with surrounding bone. The vertebral endplates (VEPs)—thin structures between the IVDs and vertebral bodies—play a critical role in moderating how mechanical loads are transferred through the spine. However, understanding how the multiscale structure and mechanics of VEPs contribute to spinal function has been limited by the challenge of linking molecular- to organ-level biomechanics.

This study combines whole-joint mechanical testing with synchrotron X-ray imaging, digital volume correlation, and X-ray diffraction to investigate how local mechanical strain, microarchitecture, mineral crystallite structure, and intrinsic prestrain interact within VEPs. The results reveal that bone and calcified cartilage within the VEP exhibit distinct mechanical behaviors—bony regions show higher tensile and shear strains, narrower mineral crystallites, and greater compressive prestrain—indicating that variations in tissue composition and structure shape how forces are distributed across the joint.

These findings mark a significant advance in our understanding of the multiscale origins of spinal joint mechanics and how micro- and nano-structural features influence load-bearing capacity. Importantly, the finding that mineral prestrain contributes to complex tissue strain patterns provides a link between nanoscale mechanics and whole-joint performance.

This work has broad implications for studying aging and pathologies such as disc degeneration and osteoarthritis, and for informing the design of orthopedic implants and biomaterials. By integrating imaging and mechanical analysis across multiple scales, the study helps bridge the gap between cell-level mechanobiology and joint-level biomechanics—offering a comprehensive framework for exploring skeletal function in health and disease.

SUMMARY

The function of all musculoskeletal joints depends on hierarchical structures spanning the molecular to whole-joint scales. Investigating biomechanics across length scales requires correlative multiscale experimental methods. This study applies multimodal *in situ* synchrotron imaging techniques to spinal

Please cite this article in press as: Parmenter et al., Variations in mineral prestrain, nanostructure, and microarchitecture play a role in intervertebral disc loading, Cell Biomaterials (2025), https://doi.org/10.1016/j.celbio.2025.100151

joints—focusing on the vertebral endplates—to explore relationships between structure and mechanical strain across spatial scales. Strain mapping using digital volume correlation combined with microarchitectural analysis reveals that high tensile and shear strains play a role in the cartilage to bone transition. Correlative imaging and diffraction show that bone contains narrower mineral nanocrystallites under greater compressive prestrain compared with calcified cartilage. We hypothesize that this multiscale structural adaptation supports the mechanical function of the intervertebral disc. Future applications of the techniques presented here have potential to help unravel the biomechanical underpinnings of pathologies affecting mineralized tissue structure. The multiscale structure-function relationships uncovered here may inspire the design of biomaterials and orthopedic implants.

INTRODUCTION

The multiscale structure of bone and cartilage underpins the biomechanical function of the musculoskeletal system. In the spine, bone and cartilage at the vertebral surface—the vertebral endplates (VEPs)—help control load and nutrient transfer from the intervertebral discs (IVDs). Back pain affects 600 million people worldwide and is the leading cause of years lived with disability (due to increase by 36% by 2050).[1] Spine biomechanics play a critical role in back pain-related pathologies such as IVD degeneration[2] and scoliosis.[3] There is therefore great interest in the biomechanics of the spine and its constituent parts, including the IVDs and VEPs,[4] which are highly complex across hierarchical spatial scales (Figure 1) and experience a large range of movements and mechanical loads in day-to-day life.

The IVD, comprising of the collagenous annulus fibrosus (AF) and proteoglycan rich nucleus pulposus (NP), deforms under loading, applying complex, location-specific strains to the calcified VEPs (Figure 1B). The IVD receives nutrition through canals in the VEPs,[5] therefore VEP structure must balance mechanical competency with permeability. The VEPs consist of calcified cartilage and bone; these mineralized tissues have differing material properties, with the elastic modulus of calcified cartilage an order of magnitude lower than bone.[6] The presence of a calcified cartilage layer between the soft tissues of the IVD and stiff vertebral bone helps create a smoother transition in material properties, reducing high strain concentrations at tissue boundaries. This greater bone stiffness persists even when mineral content is matched to calcified cartilage levels,[7] suggesting that inherent differences in non-mineralized components influences their respective mechanical properties. Raman spectroscopy has shown that there are differences in both the organic and mineral composition in calcified cartilage compared with subchondral bone in human osteochondral junctions, including higher intensity glycosaminoglycan, lipid, phosphate, and carbonate peaks in calcified cartilage.[8] Location and structure of the mineralized crystallites within the collagenous network[9–17] will play a crucial role in the local mechanical equilibrium and load transfer between the mineral and collagen, and we hypothesize that this differs between calcified cartilage and bone because of inherent differences in their organic components.

The murine VEP forms a calcified cartilage epiphysis with distinct secondary ossification (bone formation) centers, separated from the adjacent vertebral bone by a cartilaginous growth plate.[18] The formation of different musculoskeletal tissues is partly driven by the local mechanical environment.[19,20] Osteocytes in the bone compartment are considered responsive to prevailing mechanical cues and influence the three-dimensional structure of the VEPs.[21,22] Chondrocytes in cartilage are also mechanosensitive, with changes in their mechanical environment known to lead to degeneration.[23] VEP injury and degeneration disrupts the mechanical environment, driving IVD degeneration and back pain,[24,25] while VEP maintenance in health relies on the formation of optimal structures for load absorption and transfer. An appreciation of how these structures attain their function requires investigation of their biomechanics during the growth stage.

The mechanical function of VEPs is impacted by structures across spatial scales. At the macroscale, VEP thickness influences their response to load (Figure 1B). At the microscale, mineralized tissue architecture and tissue mineral density (TMD, the amount of mineral in a given volume of mineralized tissue) dominate (Figure 1C), with microstructure linked to vertebral failure.[26] At the nanoscale, mineralized collagen fibril structure (Figures 1D and 1E) and prestrain impact mechanical properties.[17,27] Prestrain—the inherent strain in a material in its undeformed state—plays a vital mechanical role[2,28,29]; loss of prestrain in the AF leads to IVD degeneration.[2] Mineralized tissue prestrain is thought to increase toughness and crack resistance[30–32] and is partly caused by the contraction of collagen fibrils during the biomineralization process.[16,33] Cells have been shown to actively generate tension in the extracellular matrix[20,34] and this may confer prestrain in the mineral. Mineral crystallites make up 40%–45% of the bone matrix volume, with the degree and nature of collagen mineralization leading to large changes in tissue mechanical properties.[27] Mineral structure across the VEPs remains unknown and we predict that this structure influences whole-joint-level biomechanics.

VEP and IVD physiology thus involves a complex feedback system between structure and mechanical forces across a range of length scales. We hypothesize that a combination of VEP microarchitecture, mineral nanostructure, and prestrain enables optimal IVD mechanical function and is partly controlled by load-induced strains *in vivo*.

Several techniques can be used to characterize biomechanics at particular spatial scales—on the whole-joint to microscale, synchrotron X-ray computed tomography (sCT) and digital volume correlation (DVC) are powerful tools for investigating the strain response of musculoskeletal tissues[35–40] and have been used to measure microscale strains in trabecular bone.[38,39] However, while DVC has been applied to study internal IVD[41,42] and

Please cite this article in press as: Parmenter et al., Variations in mineral prestrain, nanostructure, and microarchitecture play a role in intervertebral disc loading, Cell Biomaterials (2025), https://doi.org/10.1016/j.celbio.2025.100151

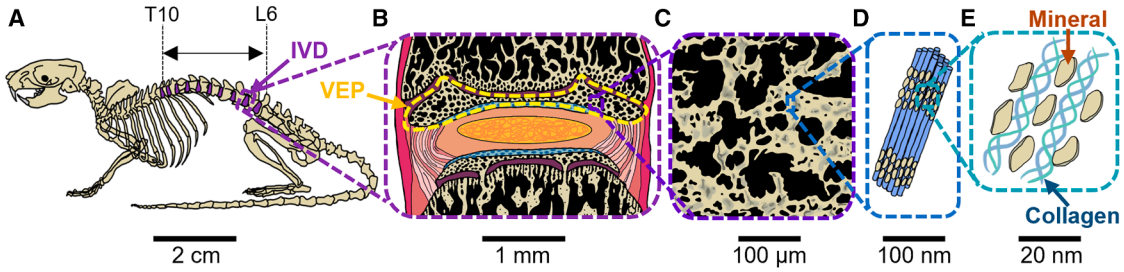

Figure 1. Structural hierarchy in the murine vertebral endplates

Illustrations of (A) the murine skeleton with IVDs investigated in this study, from thoracic vertebra 10 (T10) to lumbar vertebra 6 (L6), shown in purple; (B) the murine IVD, with cranial vertebral endplate outlined in yellow; (C) calcified tissue microstructure; (D) a mineralized collagen fibril; (E) collagen and mineral platelets.

vertebral bone[43] strains, microscale strain patterns in the VEPs have not been examined. The analysis of microscale strain fields across whole joints using DVC requires imaging with both a high spatial resolution and a large field of view (FOV). At the nanoscale, wide-angle X-ray diffraction (WAXD) can be used to quantify mineral prestrain[17] and crystallite size[14] and has been used to investigate fracture toughness in bone[44] and dentin,[30] as well as how mineral crystal structure changes with osteoarthritis.[15] 2D WAXD gives a diffraction signal with contributions from everything along the X-ray beam path, making interpretation difficult for complex, heterogeneous sample geometries. 3D WAXD methods help overcome this but require rotation of the sample around multiple axes and currently very long experimental times, making *in situ* experiments difficult.[45] There remains a need for hierarchical, multiscale imaging to bridge the gap between the cell mechanical environment and whole-joint biomechanics that can reveal the relationships between mineralized tissue prestrain and whole-joint-level mechanics. Microscale load-induced strains in the VEP during whole-IVD loading and how these strains are related to microarchitecture remain unknown, with previous mechanical studies on VEPs involving destructive sample preparation[46–48] or imaging methods unable to resolve 3D microscale features.[49–52] Variation in mineral structure and prestrain across the VEPs has not previously been measured, and the direct correlation between nanoscale mineral properties and the microarchitecture of mineralized tissues is difficult to observe.

This study aims to uncover relationships between VEP structure and mechanical strain from the nano to whole-joint scales using correlative synchrotron imaging techniques, demonstrating a novel combination of methodologies for evaluating structure-strain relationships across spatial scales. We present a series of methodological improvements for imaging whole IVD *in situ* and perform correlative sCT and WAXD of VEPs at the dual imaging and diffraction (DIAD) beamline[53] of the diamond light source (DLS) synchrotron. By combining the analysis of these two experiments, multiscale structure-function relationships can be uncovered.

We use sCT and DVC analysis to investigate whole-joint to microscale structure and mechanics in intact murine IVDs under physiologically relevant loading. We measure relative TMD, microarchitecture, and nanoscale-precision local load-induced strains to evaluate structure-strain relationships in whole VEPs. Microarchitectural values are used to determine the predominant tissue type in each region, enabling comparisons between calcified cartilage and bone without complex segmentation. Micro-to-nanoscale (Figures 1C–1E) structure and prestrain are measured by spatially correlated sCT and WAXD, to unveil relationships between microarchitecture, relative TMD, mineral structure, and prestrain. Because mineral particles are elastic and much stiffer than the organic phase (mineral Young's modulus ~100 vs. ~1–2 GPa for collagen), the stress on the mineral is proportional to the change in lattice spacing (d-period).[17] Thus, relative changes in d-period are proportional to the mineral prestrain state and are larger in regions of tensile stress and smaller in regions of compressive stress. Hence, by measuring relative changes in d-period and crystallite structure across the osteochondral junction in the VEP, we will uncover local nanoscale mechanics. These studies yield novel insights into vertebral biology and mineralized tissue biomechanics.

RESULTS

sCT resolves microscale cell-matrix organization and nanoscale-precision strains by DVC

To achieve microscale resolution of cell-matrix organization in whole IVDs under physiologically relevant loading conditions, phase contrast enhanced sCT scans of 9 murine spine segments under uniaxial compressive load were performed at beamline I13-2 at the DLS synchrotron (Figures 2A and 2B). This built on previous work[39,41,54,55] (methods), optimizing experimental parameters to improve image quality while reducing scan time and minimizing radiation dose. By imaging intact, fresh-frozen, hydrated IVDs under axial compression, the normal function of IVD structures could be observed, whereby the NP applies hydrostatic pressure in all directions, placing fibers in the AF into tension and causing the endplates to bulge outward,[56] generating compressive, tensile, and shear strains in the VEPs (Figure 2C). Four sCT scans were conducted for each sample; the first under an initial compressive preload of 1 N and the following three under cumulative displacements of 40 µm (Figure 2D). A 1.6 µm voxel size and 4.2 mm × 3.5 mm FOV enabled the microstructures of hard and soft tissues to be resolved across the entire IVD (Figures 2F and 2G). This resulted in a spatial resolution of 5.5 µm, calculated from Fourier shell correlation analysis (Note S5, Figure S3). This resolution of microscale features allowed the accurate topographical quantification of bone and calcified cartilage microarchitecture across the VEPs using commonly applied metrics (see methods). Image

Please cite this article in press as: Parmenter et al., Variations in mineral prestrain, nanostructure, and microarchitecture play a role in intervertebral disc loading, Cell Biomaterials (2025), https://doi.org/10.1016/j.celbio.2025.100151

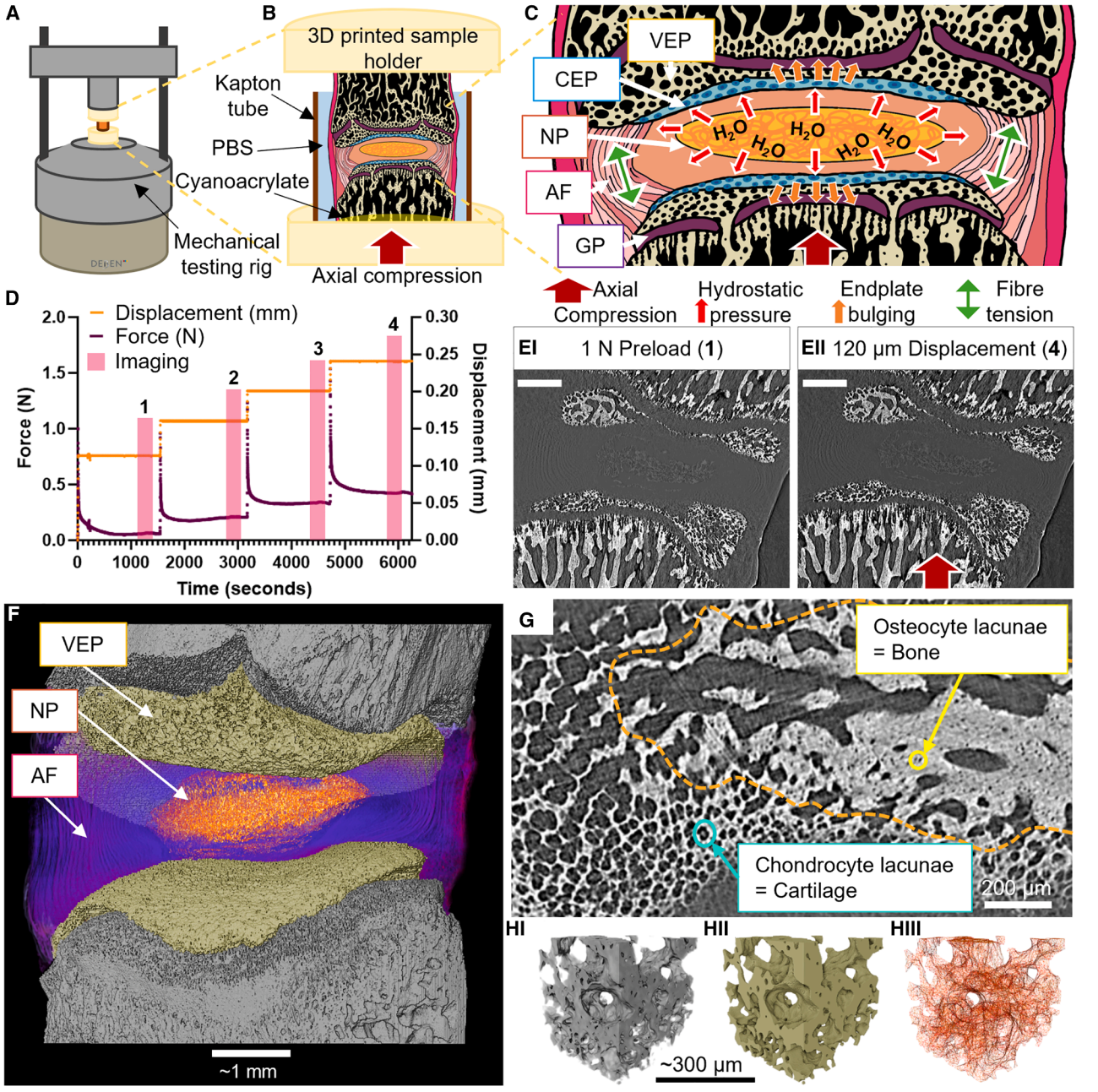

Figure 2. sCT resolves microscale cell-matrix organization and nanoscale-precision strains by DVC

(A) Schematic of the Deben CT500 mechanical testing rig and custom-built open frame with X-ray translucent carbon pillars to minimize imaging artifacts (see also Figures S1 and S2).

(B) Illustration of a cross section of the sample environment, with 3D printed sample holder, Kapton tube, phosphate buffered saline (PBS), and cyanoacrylate glue labeled.

(C) Illustration of the IVDs response to axial compression, showing hydrostatic pressure in the nucleus pulposus (NP), fiber tension in the annulus fibrosus (AF), and bulging of the vertebral and cartilage endplates (VEP and CEP respectively) into the growth plate (GP).

(D) Force and displacement readings during one loading experiment, with readings taken during scanning highlighted in pink, scan 1 was taken 20 min after application of 1 N preload, scan 2 after 40 µm compression of the IVD, scan 3 after 80 µm compression of the IVD, scan 4 after 120 µm compression of the IVD.

(E) Sagittal image slice through a sample under (i) 1 N preload, corresponding to scan 1 in (D), and (ii) 120 µm compression, corresponding to scan 4 in (D), the direction of loading is shown by the red arrow, scale bars represent 0.5 mm.

(F) 3D rendering of a whole-IVD sample, with the NP rendered in orange, AF in purple, VEPs in beige, and vertebral bone in gray, scale bar represents ~1 mm.

(legend continued on next page)

Please cite this article in press as: Parmenter et al., Variations in mineral prestrain, nanostructure, and microarchitecture play a role in intervertebral disc loading, Cell Biomaterials (2025), https://doi.org/10.1016/j.celbio.2025.100151

grayscale value (GSV) was used to approximate relative changes in TMD across the VEPs. Here, the VEPs are defined as the mineralized epiphysis between the vertebral growth plate and the IVD.

To obtain 3D strain fields across the VEP, sCT datasets were subjected to DVC analysis[36,37] using a local approach with microstructure specific point cloud (Figure 2H) and sub-voxel interpolation. This enabled the measurement of displacements with an accuracy of 10–85 nm and precision of 9–63 nm. Subsequent Lagrangian strains were calculated from the displacement field with an accuracy of 0.036%–0.09% and precision of 0.035%–0.09% (methods).

40 μm displacement applied to the sample resulted in a bulk IVD compression of 2.2% ± 0.7%, calculated from the change in distance between the VEPs (methods). In the caudal VEPs, 40 μm displacement of the sample generated local 1st principal (tensile) strains of 0.6% ± 0.3%, 3rd principal (compressive) strains of 0.7% ± 0.3%, and maximum shear strains of 0.7% ± 0.3%. In the cranial VEPs, the resulting 1st principal (tensile) strains were 0.7% ± 0.4%, 3rd principal (compressive) strains were 0.8% ± 0.4%, and maximum shear strains were 0.8% ± 0.4%.

The direction of 1st (tensile) and 3rd (compressive) principal strains with respect to the loading axis of the joint was measured as an angle between 0° (parallel to axis) and 90° (normal to axis). In the caudal VEPs, 1st principal strains were at 59° ± 0.9° and 3rd principal strains were at 54° ± 1.8° to the loading axis. In the cranial VEPs, 1st principal strains were at 59° ± 0.9° and 3rd principal strains were at 54° ± 2.6° to the loading axis. This shows that the IVD moderates the direction of strains in the adjacent mineralized tissues, potentially reducing the likelihood of vertebral compression fractures under axial loads.

The impact of radiation dose on measured strains was investigated (Note S8, Figure S6). No statistically significant changes in mean VEP strains were seen with increasing radiation dose for cumulative dose levels in the IVD equivalent to 27, 53, and 80 kGy (Figures S6A and S6B). There was no increase in the number of local strain values exceeding 10% strain, which would signify the formation of microcracks,[38] with increasing radiation dose (Figures S6C and S6D). This indicates that radiation dose had no significant impact on the results of this study.

Thickening of the peripheral endplate regions enables optimal load transfer from the IVD

To evaluate regional variations in VEP calcified tissue architecture that may modify load transfer from the IVD, sCT, and DVC datasets for each endplate ($n = 16$) were subsampled into 10 standardized cubic sub-regions (side length 325 μm) for statistical analysis of structure and strain (Figure 3A). Each of the 8 whole-IVD samples (2 endplates per sample), were treated as independent to account for variation in loading, spinal level, and image dynamics. Repeated measures correlation, which determines the common "*within sample*" association for paired measures,[57] was used to test for relationships between radial location and microarchitecture, GSV, and local mechanical strain in the sub-regions (Figure 3B). Holm-Bonferroni correction was used to deal with familywise errors,[58] and relationships were deemed significant at the 5% level. This revealed a decrease in compressive (magnitude of 3rd principal strain, $R_{rm} = -0.48$, $p < 0.001$), tensile (1st principal strain, $R_{rm} = -0.29$, $p < 0.001$), and shear strain (maximum shear strain, $R_{rm} = -0.41$, $p < 0.001$) with radial distance from the endplate center. On average, compressive strain in central endplate regions (Figure 3Ai, region 1) was 0.8% ± 0.5% higher than the outer endplate regions (Figure 3Ai, regions 4, 7, and 10), maximum shear strain was 0.6% ± 0.4% higher, and tensile strain 0.4% ± 0.3% higher after 80 μm cumulative displacement to the sample. This increase in local endplate load-induced strain below the NP agrees with previous theories that the central endplate region experiences higher strains *in vivo*[51,56] and is clearly visible in lower resolution DVC strain maps (Note S7, Figure S5).

Mineralized tissue volume fraction (MV/TV) increased with radial distance from the endplate center ($R_{rm} = 0.76$, $p < 0.001$), corresponding to an increase in thickness of the endplate toward the periphery. The degree of anisotropy was greater toward the outer endplate ($R_{rm} = 0.52$, $p < 0.001$), potentially due to the highly directional forces applied by the AF. Connectivity to mineralized tissue volume ratio (Con/MV) decreased ($R_{rm} = -0.28$, $p < 0.001$) and septal/trabecular thickness (ST.Th) increased ($R_{rm} = 0.23$, $p < 0.01$) toward the peripheral endplate, indicating a transition from calcified cartilage to bone, which can be distinguished by their resident cellular components visible in our sCT images. In bone, osteocytes reside in lacunae approximately 5 μm in diameter, in agreement with literature,[59] which reside in trabeculae 30–120 μm in thickness (Figure 2G). Calcified cartilage contains hypertrophic chondrocytes 20–50 μm in size embedded in mineralized lacunae,[60] creating a highly porous structure with mineralized cartilage septa 8–30 μm in thickness (Figure 2G). Accurate segmentation of bone and calcified cartilage in the VEPs would be extremely difficult and is not attempted in this study. Instead, microarchitectural values are used to indicate the predominant tissue type in a region, with higher values of ST.Th and MV/TV combined with lower values of Con/MV showing that a region predominantly contains bone.

Spatial mapping of VEP structure to load-induced strain reveals tension and shear as potential drivers of the cartilage to bone transition

To interrogate relationships between microarchitecture, relative TMD (approximated by GSV), and local mechanical strain, repeated measures correlation[57] was again used to test for links between the mean values for 160 endplate regions across 8 spine

(G) Grayscale cross section through a cranial VEP showing the microstructures of cartilage and bone, the bone compartment is approximately outlined in orange and identified by the presence of osteocyte lacunae, whereas the calcified cartilage contains chondrocyte lacunae, scale bar represents 200 μm.
(H) Point cloud generation for DVC, (i) grayscale 3D rendering of VEP structure, (ii) filtered and smoothed surface generated from VEP mineralized tissue structure, (iii) tetrahedral grid of the surface, the nodes of the grid are used to define the centers of the subvolumes used for DVC image tracking, scale bar represents ~300 μm.

Please cite this article in press as: Parmenter et al., Variations in mineral prestrain, nanostructure, and microarchitecture play a role in intervertebral disc loading, Cell Biomaterials (2025), https://doi.org/10.1016/j.celbio.2025.100151

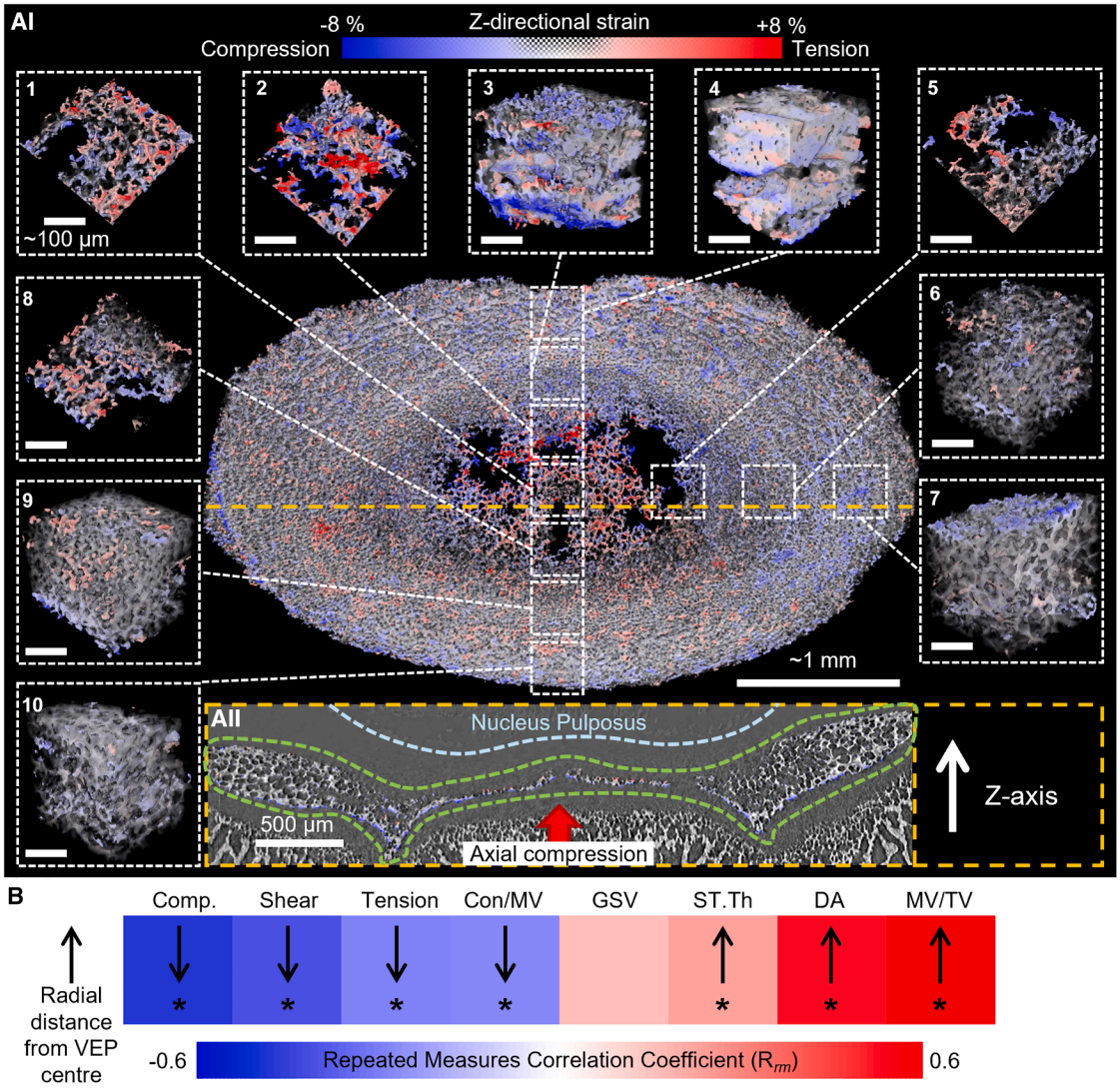

Figure 3. Thickening of the peripheral endplate regions enables optimal load transfer from the IVD

(A) (i) 3D renderings of z directional strain in a L2–3 cranial endplate. Regions used for statistical analysis are shown in dashed boxes, with scale bars representing ~100 µm; 1 = center, 2 = anterior inner, 3 = anterior middle, 4 = anterior outer, 5 = lateral inner, 6 = lateral middle, 7 = lateral outer, 8 = posterior inner, 9 = posterior middle, and 10 = posterior outer.

(ii) Grayscale image with z directional strain colorwash showing a slice through the orange dashed line on the 3D rendering in (i), the dashed green line outlines the vertebral endplate; scale bar represents 500 µm.

(B) Heatmap of repeated measures correlation coefficient (Rrm) values for mean compressive strain (Comp.), mean maximum shear strain (shear), mean tensile strain (tension), connectivity to bone volume ratio (Con/MV), mean grayscale value (GSV), mean septal/trabecular thickness (ST.Th), degree of anisotropy (DA), and mineralized tissue volume fraction (MV/TV), versus radial distance from the center of the endplate (distance defined categorically as center, inner, middle, or outer); downward arrows represent a negative and upward arrows a positive correlation; * represents statistical significance at the 5% level after Holm-Bonferroni correction (see Table S5; Figures S9 and S10 for full statistical analysis).

segments (Figure 4A). The generation and quantification of local strain induced by physiologically relevant whole-joint loading enables an examination of how the structure of a region contributes to its ability to resist load, and also how the local strains in a region may impact the formation of mineralized tissues.

Negative correlations were seen between GSV and local mechanical tensile ($R_{rm} = -0.56$, $p < 0.001$), compressive ($R_{rm} = -0.53$, $p < 0.001$), and shear strain ($R_{rm} = -0.56$, $p < 0.001$), agreeing with previous studies showing increased stiffness with higher mineralization.[61] MV/TV negatively correlated with local mechanical compressive ($R_{rm} = -0.43$, $p < 0.001$) and shear strains ($R_{rm} = -0.34$, $p < 0.001$), and ST.Th showed positive correlations with local tensile ($R_{rm} = 0.35$, $p < 0.001$) and shear strain ($R_{rm} = 0.25$, $p < 0.01$).

These correlations reveal two predominant structural types in high strain regions. First, a low TMD calcified cartilage region (identified by the presence of chondrocyte lacunae, Figure 4Biv) with low MV/TV and thin septa found in the central and inner

Please cite this article in press as: Parmenter et al., Variations in mineral prestrain, nanostructure, and microarchitecture play a role in intervertebral disc loading, Cell Biomaterials (2025), https://doi.org/10.1016/j.celbio.2025.100151

CellPress
OPEN ACCESS

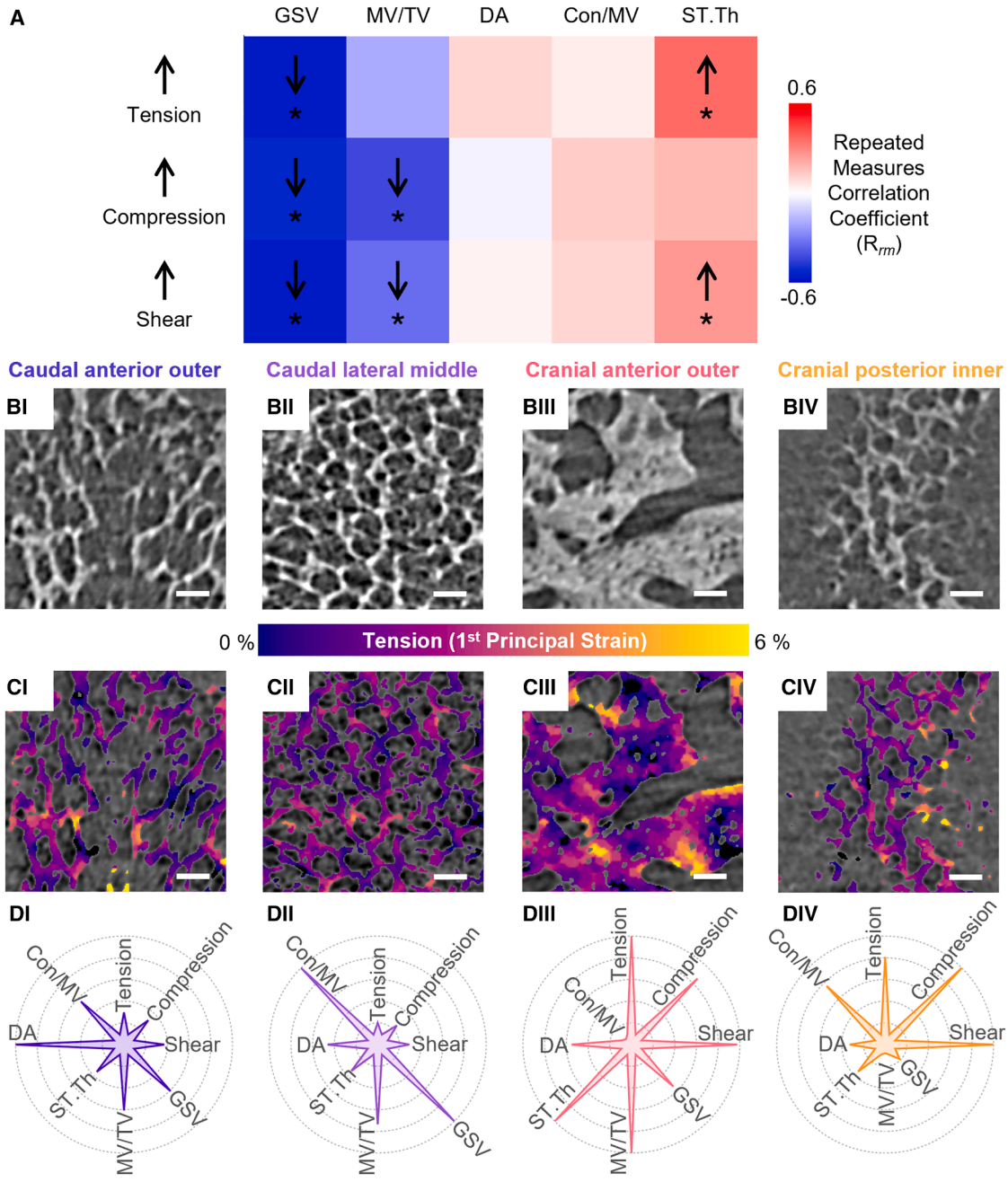

Figure 4. Spatial mapping of VEP structure to load-induced strain reveals tension and shear as potential drivers of the cartilage to bone transition

(A) Heatmap of repeated measures correlation coefficient values for image GSV, mineralized tissue volume fraction (MV/TV), DA, connectivity to mineralized tissue volume ratio (Con/MV), and mean septal/trabecular thickness (ST.Th) versus tensile strain (tension), compressive strain (compression), and maximum shear strain (Shear); * represents statistical significance at the 5% level after Holm-Bonferroni correction, full statistical results given in Table S5 and Figures S11 and S12.

(B–D) (B) Grayscale image slices, (C) tensile strain fields (compressive strain fields shown in Figure S13), and (D) radar plots of relative strains and structural parameters between 4 regions of a lumbar 4–5 sample: (i) the caudal anterior outer, (ii) the caudal lateral middle, (iii) the cranial anterior outer, and (iv) the cranial posterior inner. Scale bars represent 50 μm. Values used to generate radar plots available in Table S6.

endplate regions adjacent to the NP, which we speculate experiences elastic deformation under loading, leading to high local strains. The second type of high strain region contains trabeculae, high MV/TV, and low Con/MV, indicating that these regions have undergone endochondral ossification to form bone (confirmed by the presence of osteocyte lacunae, Figure 4Biii).

Please cite this article in press as: Parmenter et al., Variations in mineral prestrain, nanostructure, and microarchitecture play a role in intervertebral disc loading, Cell Biomaterials (2025), https://doi.org/10.1016/j.celbio.2025.100151

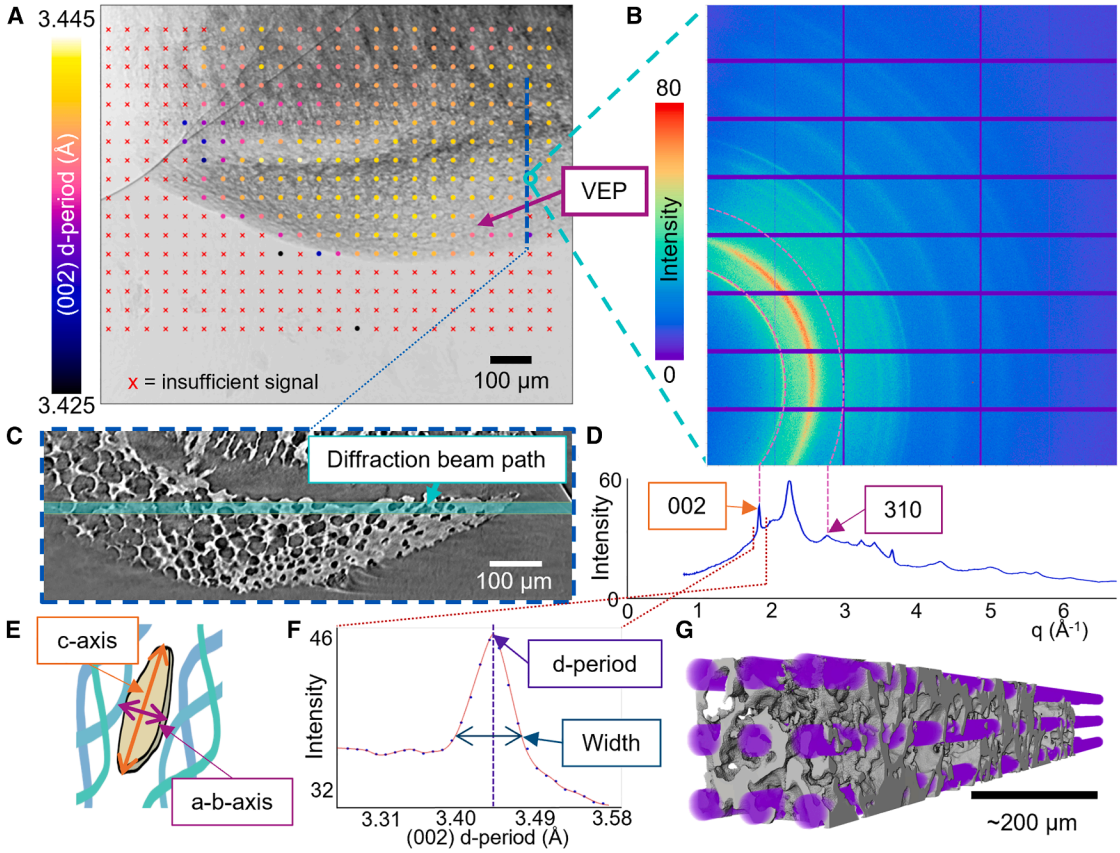

Figure 5. Correlative imaging and diffraction enable colocalization of endplate microarchitecture with nanoscale mineral crystallite properties

(A) Map of hydroxyapatite (002) lattice spacing on an X-ray projection of a quarter IVD sample held under tension, scale bar represents 100 µm (see also Figure S14).
(B) WAXD intensity pattern from the location highlighted in (A), only ~1/4 of the full diffraction rings are visible due to the need to place the WAXD detector off-center to allow for placement of the imaging camera for sCT (methods).
(C) sCT image of the endplate showing the location of the diffraction beam path that produced the WAXD pattern in (B), the location of the reconstructed slice is shown as the dashed blue line on the projection in (A), scale bar represents 100 µm.
(D) WAXD pattern in (B) integrated over q.
(E) Illustration of a mineral platelet surrounded by collagen, with *c* and *a-b* axes labeled.
(F) (002) peak plotted in d-space, with d-period and width labeled.
(G) 3D rendering of calcified tissue structure (gray) and diffraction beam paths (purple) for one region used for microstructural evaluation and statistical analysis, scale bar represents ~200 µm.

Correlative imaging and diffraction enable colocalization of endplate microarchitecture with nanoscale mineral crystallite properties

To enable colocalization of microarchitecture in VEP calcified cartilage and bone compartments with nanoscale mineral crystal properties, consecutive, spatially correlated sCT and WAXD raster scans (Figures 5A–5C) of partial IVDs was performed at the DIAD beamline, DLS[53] (methods). Physiologically relevant conditions were applied to fresh-frozen quarter IVD segments, with samples held under a tensile prestrain to simulate AF native tensile collagen prestrain and hydration maintained. The spatial resolution of sCT images was 3.2 µm, calculated from Fourier shell correlation analysis (Note S15, Figure S15). Axial and transverse d-periods were derived from the positions of the (002) and (310) WAXD peaks, respectively (Figures 5D and 5E), and mineral crystallite length and width were calculated from the corresponding peak widths[13] (Figures 5F and 5G, methods). Crystallite dimensions were 11.4 ± 1.7 nm (length) and 1.23 ± 0.13 nm (width), consistent with prior results in young, mineralized tissues.[11,62] The (002) d-period varied between 3.42 and 3.44 Å, corresponding to a variation in mineral prestrain along the *c* axis of 0.6%. The (310) d-period varied between 2.26 and 2.28 Å, corresponding to a variation in mineral prestrain along the *a-b* axis of 0.9%. Assuming a mineral Young's modulus of ~100 GPa, these prestrain variations result in 600–900 MPa prestress in the mineral.

Bone is under greater compressive prestrain and contains narrower crystallites compared with calcified cartilage

New insights into relationships between microscale VEP mineralized tissue architecture and nanoscale crystallite structure/prestrain were therefore examined by analyzing mean values of

Please cite this article in press as: Parmenter et al., Variations in mineral prestrain, nanostructure, and microarchitecture play a role in intervertebral disc loading, Cell Biomaterials (2025), https://doi.org/10.1016/j.celbio.2025.100151

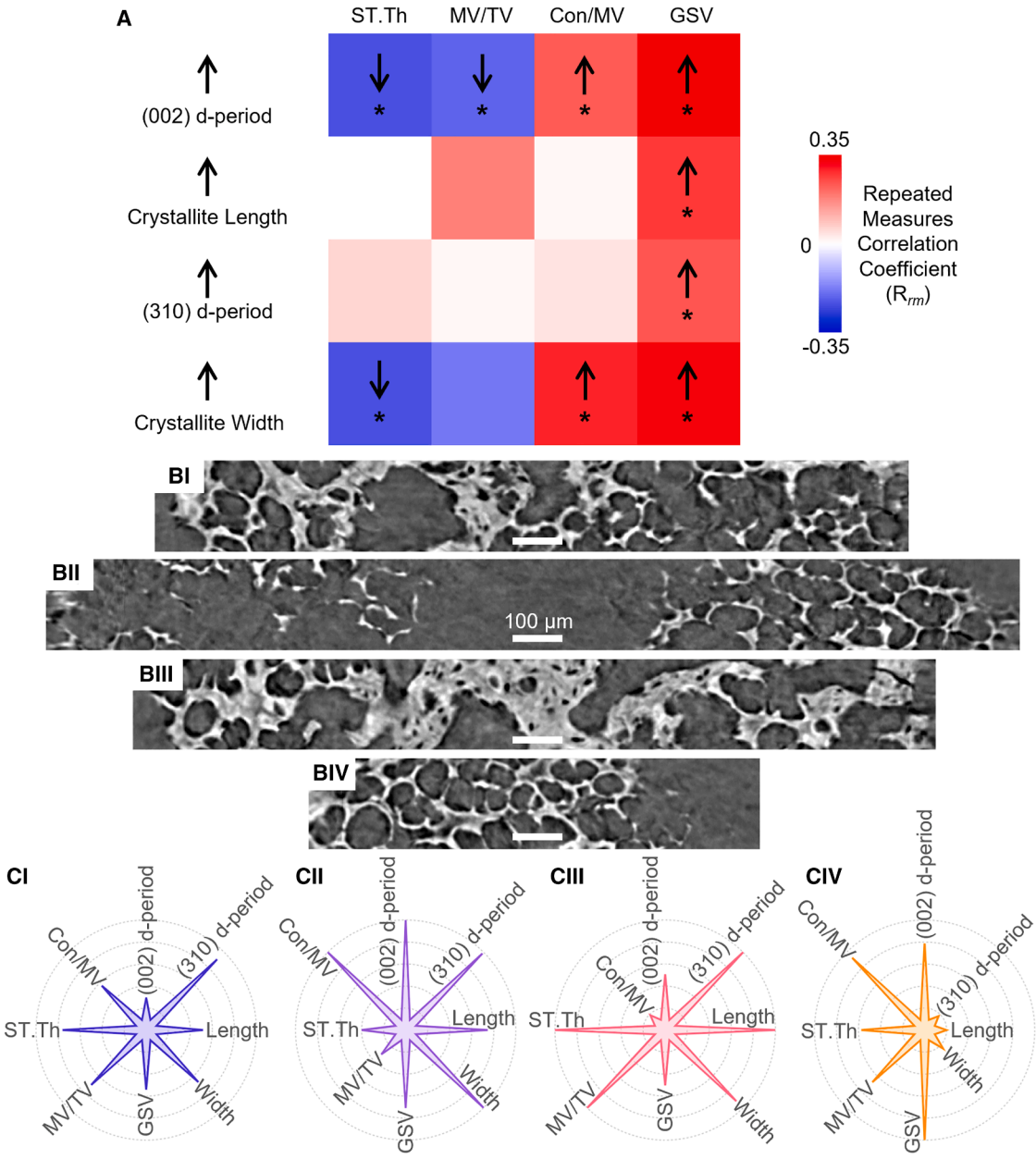

Figure 6. Bone is under greater compressive prestrain and contains narrower crystallites compared with calcified cartilage

(A) Repeated measures correlation coefficient matrix for mean septal/trabecular thickness (ST.Th), mineralized tissue volume fraction (MV/TV), connectivity to mineralized tissue volume ratio (Con/MV), and image GSVs versus mineral (002) lattice spacing ((002) d-period), mineral crystallite length (length), mineral (310) lattice spacing (310 d-period), and mineral crystallite width (width); * represents statistical significance at the 5% level after Holm-Bonferroni correction, full statistical results are presented in Table S8 and Figures S18–S20.

(B) Grayscale cross-sections from four VEP regions used for statistical analysis from one sample showing microscale structural variation in the VEP, (i) contains a mixture of calcified cartilage and bone, (ii) contains sparse calcified cartilage, (iii) consists of mostly bone, and (iv) contains calcified cartilage, scale bars represent 100 µm.

(C) Radar charts displaying the relative values of WAXD and sCT-based measurements from the four regions shown in (B) (the values used to generate the radar charts are presented in Table S9).

regions of interest (ROIs) comprising nine WAXD beam paths (Figure 5G); a total of 194 regions were taken across 8 quarter IVD samples from 4 rat lumbar spines for statistical analysis (Figures S16 and S17). Each quarter IVD sample was treated as independent and repeated measures correlation used to test for common—within sample—relationships (Figure 6A). This showed that both (002) and (310) prestrain (d-period) in the mineral was higher (more tensile) in regions with greater

Please cite this article in press as: Parmenter et al., Variations in mineral prestrain, nanostructure, and microarchitecture play a role in intervertebral disc loading, Cell Biomaterials (2025), https://doi.org/10.1016/j.celbio.2025.100151

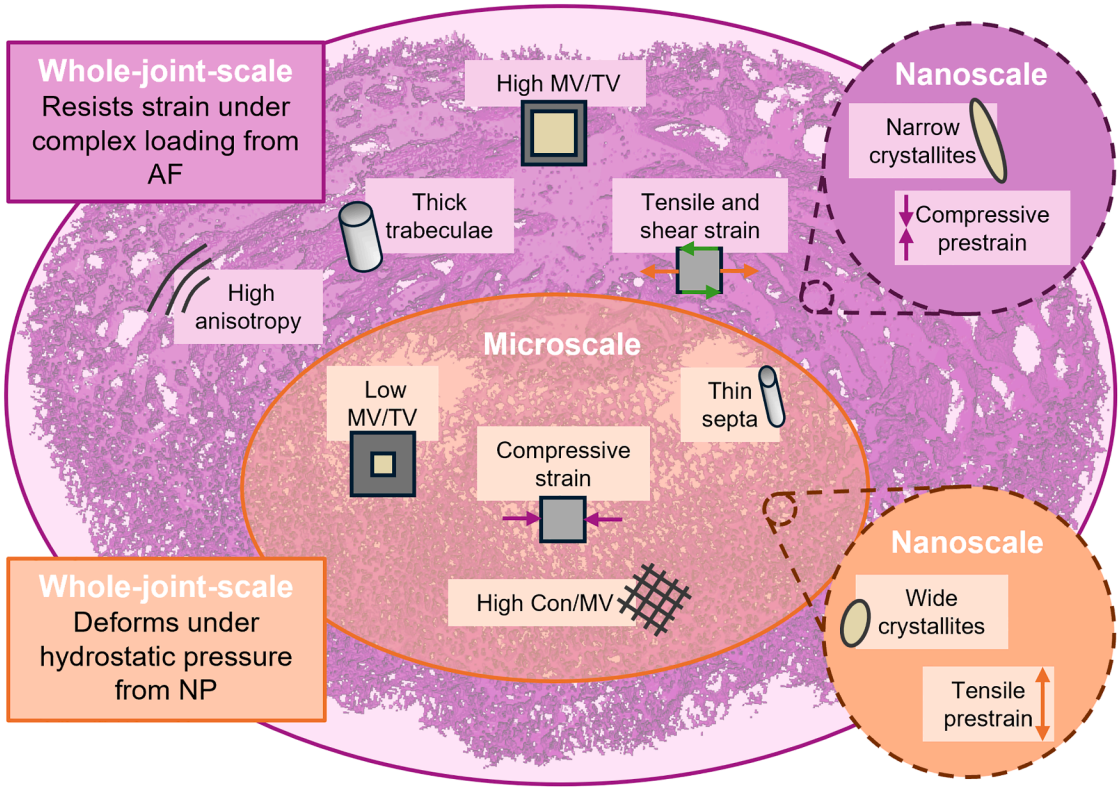

Figure 7. Summary of the differences in loading environment, structure, and prestrain between the central and peripheral vertebral endplates

At the whole-joint scale, the peripheral endplate resists complex loading from the AF; at the microscale the peripheral endplate has high anisotropy, thick trabeculae, high MV/TV (mineralized tissue volume fraction), and experiences high tensile and shear strains; at the nanoscale the peripheral endplate contains narrow mineral crystallites which are under relative compressive prestrain. The central endplate deforms under hydrostatic compressive loading from the NP; at the microscale the central endplate has low MV/TV, thin septa, high Con/MV (connectivity to mineralized tissue volume), and experiences high compressive strains; at the nanoscale the central endplate contains wide mineral crystallites which are under relative tensile prestrain.

mineralization density/GSV (R_{rm} = 0.35, $p < 0.001$; R_{rm} = 0.24, $p < 0.01$).

(002) d-period was lower in regions where structural organization indicates the presence of bone, decreasing with MV/TV ($R_{rm} = -0.21$, $p < 0.01$) and ST.Th ($R_{rm} = -0.24$, $p < 0.001$) and increasing with Con/MV (R_{rm} = 0.23, $p < 0.01$). This indicates a greater compressive prestrain in regions that have undergone endochondral ossification (such as the regions shown in Figures 5Bi and 5Biii), and that calcified cartilage is under tensile prestrain relative to bone. This supports the intriguing possibility that the local mechanical equilibrium of the mineral crystallites is functionally distinct between calcified cartilage and bone, possibly due to differences in organic composition.

Positive correlations were seen between GSV and mineral crystallite length (R_{rm} = 0.33, $p < 0.001$) and width (R_{rm} = 0.27, $p < 0.001$), confirming that more mature mineral has larger crystallites. Crystallite width decreased with ST.Th ($R_{rm} = -0.24$, $p < 0.001$) and increased with Con/MV (R_{rm} = 0.29, $p < 0.001$). This indicates that regions containing bone have narrower crystallites than regions containing calcified cartilage. Positive correlations were seen between (002) d-period and crystallite length (R_{rm} = 0.34, $p < 0.001$), and (002) d-period and crystallite width (R_{rm} = 0.44, $p < 0.001$), implying that longer, wider crystallites are formed when placed under tensile strain along the fibrillar axis, potentially due to greater alignment of gap-overlap channels in the fibril under greater tensile strain.

DISCUSSION

This study represents a step-change advance in our understanding of the multiscale origins of IVD biomechanical function, with implications for the investigation of aging and degenerative joint diseases such as IVD degeneration and osteoarthritis in future studies. The combined analysis of load-induced tissue strains using DVC and molecular-scale mineral prestrain using WAXD, has revealed the important role of mineral prestrain in forming the complex biomechanical strain patterns underpinning whole-spinal-joint-level mechanics (Figure 7). At the whole-joint scale, the decrease in overall VEP thickness adjacent to the NP enables central endplate bulging and accumulation of high tissue-level strains in these regions (Figure 7). At the microscale, higher mineralized tissue volume fraction and trabecular thickness adjacent to the AF helps resist tensile and shear strains, with these regions showing a higher degree of anisotropy

Please cite this article in press as: Parmenter et al., Variations in mineral prestrain, nanostructure, and microarchitecture play a role in intervertebral disc loading, Cell Biomaterials (2025), https://doi.org/10.1016/j.celbio.2025.100151

(Figure 7); we hypothesize that the preferential orientation of mineralized structures in these regions helps resist highly directional tensile loads from collagen fibers in the AF. The direction of tensile strains in the VEPs was 59° to the loading axis, and compressive strains 54°, demonstrating how the IVD converts axially applied loads to more radial and circumferential forces in the endplates, which we hypothesize helps prevent vertebral fracture in axial loading environments. These micro- to whole-joint-scale structure-strain relationships were conserved across all spinal levels investigated (thoracic 10 to lumbar 5). At the nanoscale, differences in prestrain and crystallite size in bone and calcified cartilage show interesting links to the strain patterns observed in whole VEPs (Figure 7). It should be noted that due to the nature of the investigation performed, only association, not causation, can be drawn from this study. Future studies should aim to test the hypotheses discussed below.

DVC found higher load-induced tensile and shear strains in regions containing bone (Figures 4Biii and 7), revealing that local mechanical strain may play a driving role in the cartilage to bone transition, providing support for the theory that hydrostatic compression inhibits endochondral ossification.[19] The microscale resolution and nanoscale precision of DVC achieved in this study enables analysis of the local cellular mechanical environment under whole-joint loading, demonstrating the potential of DVC as a tool to bridge the gap between cell mechanobiology and whole-joint biomechanics.

WAXD analysis provided nanoscale information on the structure and prestrain state of the mineral component of the extracellular matrix. Regions containing bone (Figures 6Biii and 7) showed greater mineral *compressive* prestrain which, we hypothesize, both increases VEP toughness in these regions due to mineral compaction, enabling them to resist compression with minimal deformation and allows for greater levels of tensile strain to be engendered before failure.

In contrast, VEP regions adjacent to the NP (Figure 4Biv) were shown to experience the highest tissue-level compressive strain, agreeing with theories that the endplates bulge under hydrostatic pressure from the NP.[51,56] Our WAXD analysis and quantification of mineralized tissue architectural features in these regions suggest that the mineral is instead under *tensile* prestrain relative to the bone regions mentioned previously, which may provide VEP calcified cartilage with a greater level of elastic compressibility under loading, enabling central endplate bulging to help prevent NP over-pressurization which would otherwise lead to herniation.[51] This observation of prestrain in the central VEPs is supported by experimental results in human IVDs, where the removal of the NP resulted in endplate bulging.[63] We propose that regional variations in mineralized tissue prestrain may play a vital role in the optimal mechanical function of musculoskeletal joints, and the role of prestrain in conditions such as osteoarthritis, osteoporosis, and IVD degeneration should be further investigated.

This variation in mineral prestrain in calcified cartilage and bone has an interesting correlation with similar findings of higher collagen fibril prestrains (at one step higher in the hierarchical structuring) in calcified cartilage than subchondral bone, measured from small-angle X-ray scattering (SAXS) across bovine metacarpophalangeal joints.[29] These fibrillar differences were interpreted as an adaptation in cartilage allowing for elastic deformation under compression—deforming from an initial relative tensile state to an effective zero load state when compressed. Here, the origin of the lowered mineral prestrain in bone could be explained if the collagen fibril-mineral interface is tighter than in calcified cartilage, leading to greater compressive stress exerted on the mineral platelets by the surrounding collagen (possibly due to a more organized mineral-collagen interrelationship). It has been shown that intrafibrillar mineralization generates collagen fibrillar contraction but extrafibrillar mineralization does not[33]; in the context of our results, this would imply that bone has more intrafibrillar mineralization whereas cartilage mineralization is more extrafibrillar. In this regard, these prestrain differences could also be related to the differing proteoglycan content of bone and cartilage.[8,64,65] Aggrecan, the large aggregating proteoglycan, in cartilage is known to generate a swelling pressure within the tissue, placing collagen fibers under pre-tension, and some remnants of this tensile prestrain may remain in the tissue after mineralization, resulting in a tensile mineral prestrain in calcified cartilage relative to bone. Prestrain differences could also be the result of the different cell populations in these two tissues, with different cell types actively generating differing amounts of tension in the extracellular matrix. Differing mineral substitutions between calcified cartilage and bone[8] could also result in prestrain differences by disrupting the lattice. An increase in d-period was seen with mineralization density, indicating a reduction in compressive prestrain in the mineral. This aligns with the concept of load sharing between mineral and collagen and axial fibrillar contraction,[16] which we propose leads to greater compressive load on the mineral in regions of lower TMD. Regions with more compressive mineral prestrain had smaller crystallites. Here, we have demonstrated using sCT and DVC how these variations in prestrain can be related to whole-joint mechanics, furthering the hypothesis that—at the molecular level—relative tensile prestrain in the stiff constituents of the calcified cartilage extracellular matrix enables elastic deformation under macroscale compressive load, while compressive prestrain in bone confers resistance to complex loading environments involving tension and shear.

We also observe that regions containing bone have narrower mineral crystallites than calcified cartilage regions (Figure 7), suggesting differences in mineralization between these two tissue types. Calcified cartilage contains more extrafibrillar space than bone[62] and contains mostly type II collagen rather than majority type I,[29] which may exert a role in the formation of bone apatite.[12] We speculate that the crystallites in mineralized cartilage may be wider due to their extrafibrillar, as opposed to intrafibrillar, bone-like mineralization.[11,66] Mechanically, computational modeling has shown that plastic spreading of crystallites first occurs in the extrafibrillar space, followed by the intermolecular space,[67] so differences in mineral location between calcified cartilage and bone would result in differing material properties. Osteoblasts in bone and chondrocytes in cartilage have different directional preferences for the initiation of mineralization by matrix vesicle secretion,[68] and we hypothesize that this may also play a role in the differences in crystallite shape observed in this study. Studies have shown that crystallites with larger aspect ratios increase the stiffness, strength, and toughness of

Please cite this article in press as: Parmenter et al., Variations in mineral prestrain, nanostructure, and microarchitecture play a role in intervertebral disc loading, Cell Biomaterials (2025), https://doi.org/10.1016/j.celbio.2025.100151

mineralized tissues,[69,70] and the wider mineral crystallites in calcified cartilage would have a lower aspect ratio. The variation in prestrain and crystallite shape seen here may explain why bone is stiffer and harder than calcified cartilage even when their mineral content is similar[7] and supports the notion that calcified cartilage acts as an important transition layer in diarthrodial joints, reducing the strains generated at hard-soft tissue boundaries.[6,29,62] Changes in mineralization and mineralized tissue structure are associated with multiple pathologies, including osteoarthritis[8,15] and IVD calcification,[71] and the combination of methods presented in this study should be used to investigate these conditions in future studies.

This study demonstrates that regional variations in multiscale structure and strain at the joint articulating surface contribute to overall mechanical performance. These regional variations should be considered when designing orthopedic implants and biomaterials, for example gradient scaffolds. Gradient scaffolds for osteochondral repair improve repair and regeneration compared with homogeneous scaffolds but still require improvement for clinical translation.[72] Improvements in manufacturing methods such as 3D printing means that producing biomaterials with varying microarchitectures is becoming more common,[73] and the microarchitectural relationships uncovered here should be used to inform the design of novel biomaterials. As nanostructured materials are showing huge promise for orthopedic biomaterials development,[74] we propose that the introduction of a nano-crystallite size/shape gradients and molecular level prestrain may improve the functionality of biomaterials for orthopedic applications.

The rat model used here is considered representative of young, healthy IVD and was chosen primarily based on size with respect to the imaging FOV available in this study and because of its common use in preclinical research. Rat lumbar disc geometry resembles human discs, so is suitable for the investigation of axial mechanics.[75] The young age (8 weeks) of the animals was chosen to enable investigation of mineralized structures that form during the growth stage, and it should be noted that the structure-strain relationships uncovered in this study may change with age as mineralized structures further adapt to their mechanical environment. Future studies should investigate how these relationships change with age and degenerative conditions including osteoarthritis and IVD degeneration.

Limitations of this study include scan times, radiation dose, and the need to perform two separate experiments. The 3-min scan times used for whole-IVD *in situ* imaging meant that truly dynamic imaging was not possible. The quasi-dynamic regime used was able to capture load-induced strains after full stress relaxation, meaning a significant proportion of strain was taken up by the soft tissues of the IVD. Dynamic mechanical responses occurring during and immediately after loading could not be captured in this study, and it is likely the mineralized tissues experience higher strains immediately after the load is applied, making our results a lower bound. Scan times on the order of seconds have been achieved to dynamically investigate cartilage biomechanics,[40] and future studies of the IVD should look at utilizing similar fast imaging setups. The accuracy of the load cell used in this study (±1 N) was insufficient for the collection of reliable force data and means there was likely variability in sample preload, this was accounted for statistically by treating each mechanical experiment, consisting of preload plus three displacement steps, as independent. An absolute pixelwise quantification of TMD was not possible from the images used in this study due to phase contrast effects, and there is ongoing discussion around the relationship between GSVs from Paganin filtered phase contrast enhanced images and TMD (Note S10, Figure S8). However, by taking mean regional values from Paganin filtered images it was possible to approximate relative changes in TMD within a sample.

Radiation dose can cause a change in the elastic properties of bone and induce microcracking,[76] so attempts were made to reduce radiation dose during all experimental procedures. The applied dose per image during *in situ* sCT was 27 kGy, below the 35 kGy often quoted as safe for bone samples,[77] and studies on cartilage biomechanics have shown no clear radiation dose effects on *in situ* mechanics at doses up to 300 kGy.[40] Here, no changes in measured strain values in the VEPs were seen with increasing radiation dose (Figure S6), so it can be concluded that radiation dose did not have a statistically significant impact on the results of this study.

The WAXD patterns collected in this study covered only a quarter of the azimuthal range, preventing the analysis of crystallite orientation. This study used 2D WAXD analysis, but 3D diffraction techniques can provide a fuller picture of how nanoscale structure and prestrain change throughout complex sample geometries.[45] The tensile preload applied to partial IVD samples during correlative sCT and WAXD was designed to mimic physiological conditions, but this may have resulted in some load-induced strain in the mineral as opposed to purely prestrain. However, the maximum load-induced strain seen in the mineral portion of bone during elastic loading is around 0.2%,[17,77] so the ~1% variation in mineral strain seen in this study must be predominately due to prestrain effects. This study used two separate beamlines to achieve both *in situ* sCT of whole-joint loading and correlative sCT and WAXD; ideally, a beamline setup enabling simultaneous acquisition of both datasets should be used.

Conclusions

Combined sCT, DVC, and WAXD analyses have enabled whole-joint to nanoscale structural quantification of murine VEPs, showing significant radial variation, transitioning from a thin layer of calcified cartilage centrally, adjacent to the NP, to thicker peripheral bone structures close to the AF (Figure 7). DVC enabled quantification of 3D strain fields in VEP microarchitectures, revealing the presence of higher load-induced strains in the central VEPs adjacent to the NP. Regions containing bone had higher loading-related tissue-level tensile and shear strains, potentially demonstrating the instructive role of mechanical loading in the cartilage to bone transition, with complex loading environments involving tension and shear leading to bone formation and hydrostatic compressive environments remaining as cartilage. Correlative sCT and WAXD exposed divergent mineral prestrain in bone and calcified cartilage, with calcified cartilage under tensile prestrain relative to the compressive prestrain of bone regions (Figure 7). Regions containing bone had narrower crystallites compared with calcified cartilage, which likely indicates that cartilage undergoes more extrafibrillar mineralization. Mineral crystallites were both longer and wider when under

Please cite this article in press as: Parmenter et al., Variations in mineral prestrain, nanostructure, and microarchitecture play a role in intervertebral disc loading, Cell Biomaterials (2025), https://doi.org/10.1016/j.celbio.2025.100151

relative tensile prestrain. Linking these nanoscale results back to the structure and function of the VEPs, we hypothesize that compressive prestrain and a higher crystallite aspect ratio in the bone around the peripheral VEPs aids in resisting complex loading from the AF, whereas tensile prestrain and a low crystallite aspect ratio in the calcified cartilage below the NP enables its elastic deformation under hydrostatic compression and prevents NP over-pressurization.

Our data demonstrate the potential of *in situ* multimodal X-ray probing for multiscale biomechanics and mechanobiology. Each modality offers a unique complementary dataset, allowing a holistic approach to interpreting biomechanics from the whole-joint to molecular scales. Future applications of these techniques have the potential to unravel the biomechanical underpinnings of biomineralization, growth, aging, and the effects of pathologies known to affect mineralized tissue structure, including osteoarthritis and osteoporosis. The multiscale structure-function relationships uncovered here should be used to inform the design of novel biomaterials.

METHODS

Animals and sample preparation

Male 8-week-old Sprague Dawley rats kept in controlled conditions (12:12 h light:dark cycles, 22°C and *ad libitum* access to food and water) at the University of Manchester Biomedical Sciences Facility with all tissue collection procedures performed in accordance with the UK Animals (Scientific Procedures) Act 1986, local regulations set by the UK Home Office with institutional approval obtained from the University of Manchester Animal Welfare and Ethics Review Board under the Home Office Licence (#70/8858 or I045CA465). Whole spines were dissected and snap frozen in liquid nitrogen prior to storage at −80°C. Within 24 h of *in situ* mechanical testing, samples were thawed at room temperature before further dissection.

For *in situ* sCT of whole IVD, 9 individual spinal units across 3 spines (from vertebral levels thoracic 9 to lumbar 6) consisting of an IVD with half vertebrae either side and posterior elements removed were used for analysis (sample information given in Note S1 and Table S1). Removal of posterior elements was required to enable visualization and isolation of the IVD. Dissections were performed using a high precision diamond cutting blade (Accumtom-50; Struers, UK). Sample damage was minimized during dissection through the use of water cooling, a slow feed speed (0.05 mm/s) and 1,800 rpm. Spinal level was recorded in terms of vertebral number either side of the IVD for each sample (Table S1).

For correlative imaging and diffraction experiments, spinal units from spinal levels lumbar 3 to lumbar 6 were further dissected into quarters along the spinal axis, resulting in 8 partial vertebra-annulus-vertebra samples from 4 spines used for analysis (sample information given in Note S13 and Table S7). This was done to ensure samples fitted within the smaller imaging FOV at the DIAD beamline (1.38 mm × 1.16 mm).

In situ mechanical testing

Samples were mounted in a Deben CT500 (Deben, UK) rig containing a 100 N loadcell (accuracy ±1% of full scale) and custom-built open frame design consisting of an aluminum alloy base cover and two carbon fiber pillars bridged by an aluminum alloy crossbar. The rig had a 10 mm linear extensometer for position readout, with a 3 μm resolution, and linearity 1% of full scale. The open frame design gave easy access to the samples during alignment and rehydration and reduced the amount of material in the path of the diffraction beam for DIAD experiments. Custom 3D printed (Acrylonitrile Butadiene Styrene, ABS) sample holders were used for sample mounting.

For *in situ* sCT of whole IVDs, spinal units were fixed to the bottom 3D printed compression plate using superglue (Vetbond, 3M) and left free at the top. Samples were placed inside polyimide tubing (diameter 6 mm, wall thickness 75 μm) filled with phosphate buffered saline (PBS) to maintain sample hydration during scanning (Figure S1). Samples were held under cumulative axial compression, applied in the z direction from beneath the bottom sample holder during imaging. A 1 N compressive preload was first applied, corresponding to approximately 40% the animal's body weight (260 ± 33 g), designed to prevent over swelling of the NP and generate a physiologically relevant level of intradiscal pressure by simulating super-incumbent body weight.[56] The first sCT image was taken 20 min after application of the preload to allow for stress relaxation and reduce motion artifacts acquired during scanning. Three further images were taken after applying successive 40 μm displacement steps. Peak and relaxed load readouts for each sample are given in Table S2. All loads and displacements were applied at a slow rate of 0.1 mm/min to reduce the amount of stress relaxation after loading. The full force, displacement, time readout for one experiment (sample 5) is available in the supplemental dataset (FigShare: https://doi.org/10.5522/04/26789212).[78]

For correlative imaging and diffraction experiments, partial vertebra-annulus-vertebra samples were fixed at both ends to 3D printed sample holders using superglue (Vetbond, 3 M). Samples were placed inside polyimide tubing (diameter 4 mm, wall thickness 76 μm) filled with PBS to maintain sample hydration during scanning (see Note S14 and Figure S14). A 2.5 N tensile preload was applied before scanning to place annulus fibers into tension and prevent sample motion during scanning. sCT scanning was performed after 30 min stress relaxation, followed by WAXD scans.

Phase contrast enhanced sCT imaging of whole IVD

sCT of whole IVDs was performed at the Diamond-Manchester Imaging Branchline I13-2[79] at DLS, UK using a pink beam with mean energy 27.6 keV. Low energy X-rays were removed using filters (Pyr. Graphite 0.28 + 1.06 mm, Al 3.2 mm, Fe 0.14 mm) to reduce radiation dose to the samples. Imaging setup (Figure S1) was based on previous experiments,[55] with the main changes being a more efficient scintillator, 500 μm LuAG SO14, and a larger propagation distance of 0.5 m, allowing shorter exposure times to be used (Note S2). 1,800 projections with 0.1 s exposure time were taken per image volume using fly scanning, resulting in a scan time of 3 min and an applied X-ray dose of 27 kG, an 85% reduction in dose compared with previous experiments,[54] see Note S4 for full calculation. Images had a 1.6 μm voxel size and 4.2 mm × 3.5 mm FOV. Limited angle tomography artifacts resulting from the open frame mechanical testing rig were

avoided through the use of carbon fiber pillars which were designed to be X-ray transparent, allowing collection of usable tomographic projections at all angles. One pillar covering the FOV results in a 22% loss of intensity at the detector, and the pillars appear in 19% of the collected projections (Note S3, Figure S2). No correction for this loss of intensity was made during image reconstruction.

Tomographic datasets were reconstructed using the open-source pipeline Savu.[80] First, projections were pre-processed using flat and dark-field correction and lens distortion correction,[81] followed by ring artifact removal.[82] Datasets were then reconstructed using the filtered back projection algorithm[83] with Paganin phase retrieval[84] (δ/β value of 100) formatted in 16-bit tif stacks. An unsharp mask (radius = 2.5 pixels and weight = 0.9) was applied to the reconstructed datasets using ImageJ[85] to reduce blurring associated with applying a Paganin filter. The Paganin filter acts as a low pass filter, improving image contrast while retaining the same absorption-contrast information[86] (Figure S8). Example sCT images are available in the supplemental dataset.[78] The spatial resolution of the images was determined using Fourier shell correlation analysis (Note S5, Figure S3).

Point cloud generation for DVC

The DVC point cloud specifies the location of the center of each subvolume used for tracking. Point clouds for the VEPs were created using interactive thresholding and meshing in Avizo 2022.2 (Thermo Fisher Scientific, Waltham, Massachusetts, USA) (Figure 2H). Here, the VEPs are defined as the epiphysis between the vertebra and the IVD (Figure 3Aii). The interactive thresholding tool was used to create a binary image of the calcified tissue regions. The threshold value was chosen for each image individually, based on the value best able to separate mineralized tissue from the marrow space. The volume edit tool was then used to remove the underlying vertebral bone and ensure points could not be placed too close to the edge of the image or in regions severely affected by imaging artifacts. The Remove Small Spots module was used with size 2×10^7 3D to remove any disconnected regions from the binary image. The Remove Small Holes module was used with size 14,000 3D to remove holes smaller than the DVC subvolume size. A Binary Smoothing was applied with a kernel size of 3 in all directions and threshold of 0.55, this slightly eroded the binary image away from the edges of the mineralized tissue and smoothed the image to improve meshing. A surface was then generated from the smoothed binary image and the surface simplified by increasing the minimum distance between nodes to 4.5 voxels (7.3 μm). A tetrahedral grid was generated from the surface and the nodes of the mesh used to specify locations of the points used for DVC (Figure 2H). This resulted in highly dense point clouds containing ~1 million points per endplate, resulting in a subvolume overlap of up to 80%. VEP meshes and point clouds for sample 5 are available in the supplemental dataset (FigShare: https://doi.org/10.5522/04/26789212).[78]

DVC

DVC was performed using the local approach with flexible point cloud specification.[36,37] Source code was supported by CCPi (Collaborative Computational Project in Tomographic Imaging, https://tomographicimaging.github.io/iDVC/, v.21.1.0). All DVC computations were run using spherical subvolumes with 12 degrees of freedom (translation, rotation, and 1st order strain), using a zero-normalized sum-of-square difference (ZNSSD) function for optimization. A subvolume diameter of 30 voxels (49 μm) was used with 2,000 sampling points per volume. GSV was interpolated within subvolumes at these sampling points using tricubic interpolation, enabling subvoxel displacement measurements. Lagrangian strains were calculated from the displacement field using polynomial fitting and differentiation.[37] A strain window of 25 points was used, resulting in a mean strain window radius of 21.4 μm, calculated as:

$$\textit{Strain window radius} = d \times \sqrt[3]{n}$$

Where d is the mean distance between points in the point cloud (here 4.5 voxels) and n is the number of points used for polynomial fitting in the strain calculation (25). This resulted in a virtual strain gauge length of 91.5 μm, representing the span of points used in the strain calculation, calculated as the strain window diameter plus the subvolume diameter.

Accuracy and precision of the displacement and strain fields were calculated using a zero-strain analysis. Standard zero-strain analyses involve using two images taken sequentially of a sample without applying any load. This method can be problematic when imaging highly viscoelastic samples such as the IVD, as they are likely to have moved between scans, wrongly giving the impression of poor DVC accuracy and precision. An alternative zero-strain method was used for this experiment, where one scan was taken with 3,600 projections, which was then split into two sets of 1,800 projections to be used for zero-strain analysis.[54] This produces two independent scans taken at the same time, removing the potential impacts of viscoelasticity and providing a more robust method of determining true DVC accuracy. Images for zero-strain analysis were reconstructed without projections containing carbon pillars, using ~1,600 projections. This was done to prevent differences between the two images caused by the carbon pillars appearing in slightly different locations between the two scans. A point cloud was created for the cranial endplate of one lumbar 1–2 sample containing 1,067,120 measurement points.

Strain accuracy and precision were calculated as the mean absolute error (MAER) and standard deviation of error (SDER) as described by Liu and Morgan.[87]

$$MAER = \frac{1}{N}\sum_{k=1}^{N}\left(\frac{1}{6}\sum_{c=1}^{6}\left|\varepsilon_{c,k}\right|\right)$$

$$SDER = \sqrt{\frac{1}{N}\sum_{k=1}^{N}\left(\frac{1}{6}\sum_{c=1}^{6}\left|\varepsilon_{c,k}\right| - MAER\right)^2}$$

And analogously for the displacements, where N represents the number of points, k is the point in the point cloud, c is the

Please cite this article in press as: Parmenter et al., Variations in mineral prestrain, nanostructure, and microarchitecture play a role in intervertebral disc loading, Cell Biomaterials (2025), https://doi.org/10.1016/j.celbio.2025.100151

component of strain, and ε is the strain value. Displacement MAER was 10 nm and SDER was 9 nm, strain MAER was 0.036% and SDER was 0.035% (full data shown in Figure S4A). The objective minimum values (resulting from minimization of the ZNSSD function[37]) from DVC were $2.6 \times 10^{-4} \pm 3.1 \times 10^{-4}$.

A standard zero-strain analysis, where two scans were performed sequentially without applying any load to the sample, was performed to test the overall accuracy and precision of the *in situ* imaging setup using one lumbar 3–4 sample. A point cloud was generated for the cranial endplate consisting of 1,150,301 points and used for DVC. This gave a displacement accuracy of 85 nm, displacement precision of 63 nm, and strain accuracy and precision of 0.09% (full data shown in Figure S4B). The objective minimum values from DVC were $7.0 \times 10^{-4} \pm 3.5 \times 10^{-4}$.

The 1st and 3rd eigenvalues of the strain tensor were calculated and used for measurements of tensile and compressive strain, respectively. Maximum shear strain was calculated as: $\tau = \frac{\varepsilon_1 - \varepsilon_3}{2}$, where τ is maximum shear strain, ε_1 is 1st principal strain, and ε_3 is 3rd principal strain. Mean strain values for each endplate are given in Table S3. Mean objective minimum values from DVC are given in Table S4.

Bulk IVD strain was calculated from the change in mean distance between the cranial and caudal VEPs. Initial IVD height was calculated as the distance between the mean (x, y, z) coordinates of the cranial and caudal DVC point clouds. IVD height after each displacement step was calculated by adding the DVC displacements to each point in the point clouds and calculating the new distance between the mean values. The percentage change in height was calculated to give bulk IVD compressive strain (Matlab code provided in Note S6), and the values for each sample are given in Table S3.

To determine the direction of strains in the VEP with respect to the loading axis of the joint, the angles between the 1st (tensile) and 3rd (compressive) strain eigenvectors and the z axis was calculated from 0°–90°, whereby 0° represents strains acting parallel to the loading axis and 90° strains acting orthogonal to the loading axis. Angles were calculated for each point in the DVC point cloud (Matlab code provided in Note S6), and the mean values reported in results and Table S3.

Correlative imaging and diffraction

Spatially correlated sCT and WAXD were performed at the DIAD beamline, DLS[53] (Note S14, Figure S14). sCT data was acquired using a pink beam filtered with a Pt strip and 4 mm Al to give a mean beam energy of ~27 keV. An additional 1.4 mm Al and 0.2 mm Cu were used during sample alignment to reduce X-ray dose on the sample. Sample to detector distance was set to 150 mm. Images were collected using scintillator-coupled optics and a PCO.edge 5.5 camera (Excelitas Technologies, Waltham, MA 02451), with a voxel size of 0.54 μm and a FOV of ~1.38 mm × 1.16 mm. 2,500 projections from 0 to 180° with a 50 ms exposure time were collected per scan. 20 dark- and 20 flat-field projections were collected at the start and end of each scan for background correction. Images were reconstructed in Savu using filtered back projection, a Fresnel filter, and an unsharp mask. Spatial resolution of the images was determined using Fourier shell correlation analysis (Note S15, Figure S15).

A 17 keV diffraction beam with a 25 μm × 25 μm spot size was used for collection of WAXD data. Data was collected with a PILATUS3X CdTe2M detector (pixel size 172 μm × 172 μm, Dectris AG, Baden-Daetwill, Switzerland) with an angular position (relative to the sample) covering an azimuthal (χ) range of approximately −67° to 27°, and a sample to detector distance of 32.5 cm, determined through calibration with LaB_6.[88] Diffraction mapping of the endplate was done on a grid of 24 × 17 points with a horizontal step of 54 μm and vertical step of 51 μm, 5 s exposure time was used per point.

WAXD analysis

WAXD data was processed using moving beam azimuthal integration in the DAWN[89] (v.2.33) software package. Azimuthal range was constrained to −67° to 27°, and radial range between 0.79–7.00 $Å^{-1}$ with a binning value of 1,000 (including pixel splitting). Resulting one-dimensional datasets of q versus scattering intensity were analyzed using custom designed programs[78] in Python (v.3.10) (FigShare: https://doi.org/10.5522/04/26789212). In each dataset, the (002) peak was isolated by subsampling scattering intensity for q values between 1.75–1.9 $Å^{-1}$. Peaks were modeled by fitting with a Gaussian function using the library for least squares minimization and data fitting (LMFIT) Python library,[90] and only points with fitted peak area greater than 5 (in intensity units) were recorded. For these models, (002) d-period was estimated from the model center q_0 along q ($Å^{-1}$) by the equation $d(002) = 2\pi/q_0$; peak height was estimated as the model amplitude; and peak width was taken as 6σ where σ is the width term in the Gaussian function. This same method was repeated for the (310) peak, selecting the q range between 2.63–2.89 $Å^{-1}$ and changing the fitted peak area threshold to greater than 30 intensity units (reflecting the higher absolute intensity values of this scattering region in mineralized tissues). For each WAXD map, nanoscale properties were mapped onto two-dimensional images of sCT reconstructions, summed across their x axis, using the saved motor positions for each WAXD beampath.

Crystallite length and width were calculated from the 002 and 310 peaks respectively, using the following equation:

$$L = \frac{K\lambda}{B(2\theta)\cos\theta}$$

Where L is the crystallite size, K is a dimensionless shape factor ($K = 0.9$), λ is the wavelength of the X-ray beam ($\lambda = 0.7348$ Å), B is the peak width, and 2θ is the Bragg angle.[91]

Regionalized analysis of microstructure, relative TMD, and DVC strain from sCT data

ROIs were taken from the sCT datasets for microstructural analysis and quantification of GSV. For whole-IVD datasets, 200 voxel (325 μm) cubed ROIs were chosen at 10 anatomical locations in each endplate (see Figures 3A and S7; Note S9) across 8 samples, resulting in 160 regions. For correlative imaging and diffraction experiments, ROIs comprising nine diffraction beam paths were used (Figure 5E), resulting in 125 μm × 120 μm

CellPress
OPEN ACCESS

Cell Biomaterials
Article

rectangles projected through the width of the sample. 15–32 regions were taken across 8 samples, resulting in 194 regions for statistical analysis (see Note S16 and Figures S16 and S17).

Endplate microstructure was binarized using the interactive thresholding module in Avizo, and ROIs were taken using the extract subvolume module. Grayscale images were masked with the binarized calcified tissue microstructure and mean GSV for each ROI was calculated as a representative value for TMD. There was significant variation in GSVs between samples, due to differences in the minimum and maximum intensity of X-rays hitting the detector for each sample, which determines the final image histogram; factors that influence this are sample size and the presence of air bubbles. This meant that inter-sample variation in TMD could not be analyzed. Binary images were saved as 3D Tiffs and opened in ImageJ for microstructural quantification using BoneJ (BoneJ2 release 7.0.18).[92] Mineralized tissue volume fraction (MV/TV) was calculated using the area/volume fraction module. Osteocyte lacunae were removed from the images using a maximum followed by a minimum filter (size = 2.5 voxels for I13 sCT data, size = 8 voxels for DIAD sCT data). Mean septal/trabecular thickness (ST.Th) was calculated using the thickness module in BoneJ.[93,94] Degree of anisotropy was calculated using the anisotropy module[95,96] with 2,000 directions, 10,000 lines, and a sampling increment of 1.73; anisotropy was not analyzed for DIAD data due to the inherent anisotropy in the shape of the ROIs analyzed. Purify was run on the regions to ensure the presence of a single connected structure before running the connectivity (Modern) plugin[97,98] to calculate the connectivity of the ROIs, this was then divided by mineralized tissue volume to give connectivity to mineralized tissue volume ratio (Con/MV).

Mean values of DVC measured strain were calculated for each ROI in the whole-IVD datasets. Tensile strain (tension) was calculated as the mean 1st principal strain, compressive strain (compression) was calculated as the magnitude of mean 3rd principal strain, and shear strain (shear) was calculated as the mean maximum shear strain in the region.

Statistical analysis

Statistical analysis was applied to the mean values from ROIs for each dataset: 160 regions from *in situ* sCT imaging data and 194 regions from correlative imaging and diffraction data. Repeated measures correlation was performed using the rmcorrShiny app[99] and used to determine common intra-sample associations without violating assumptions of independence of observations,[57] with data grouped by sample (whole or quarter IVD). Each sample was treated as independent to account for variations in mechanical loading, differences in image histograms and subsequent thresholding of microstructure, and the fact that samples from the same animal were from different spinal levels and therefore anatomically distinct. Whole-IVD samples for *in situ* sCT data each had 20 regions (Note S9, Figure S6), and quarter IVD samples for correlative sCT and WAXD had 15–32 regions depending on sample geometry (Figures S14 and S15). The Holm-Bonferroni method was applied in Microsoft Excel and used to deal with familywise error rates,[58] and target p value set to 0.05. Full datasets used for statistical analysis are available in the supplemental dataset (FigShare: https://doi.org/10.5522/04/26789212).[78]

RESOURCE AVAILABILITY

Lead contact

Further information and requests for data should be directed to and will be fulfilled by the lead contact, Alissa Parmenter (alissa.parmenter.20@ucl.ac.uk).

Materials availability

This study did not generate new unique reagents.

Data and code availability

- Supplemental data have been deposited at Figshare and are publicly available as of the date of publication at https://doi.org/10.5522/04/26789212.
- The complete dataset, of considerable size, will be shared by the lead contact upon reasonable request.
- All original code has been deposited at Figshare at https://doi.org/10.5522/04/26789212 or is included in the supplemental information.

Example datasets are available on Figshare (Parmenter et al.[78]). Supplemental data: Variations in mineral prestrain, nanostructure, and microarchitecture play a role in intervertebral disc loading. University College London. Dataset. https://doi.org/10.5522/04/26789212). All data (of considerable size) is available from the corresponding authors upon reasonable request.

ACKNOWLEDGMENTS

Laboratory space and facilities were provided by the Research Complex at Harwell. We thank S. Marussi for his support with the adaptation of the mechanical testing rig. We acknowledge the University of Manchester at Harwell for providing the mechanical testing rig. We thank M. Sherratt for providing samples. We thank J. Brunet, J. Liu, S. Rahmani, S. Marathe, J. Chen, and Y. Zhou for their help on beamtimes. We acknowledge funding from the UK Engineering and Physical Sciences Research Council (EP/V011235/1 and EP/V011006/1), UK Medical Research Council (MR/R025673/1 and MR/V033506/1), Royal Academy of Engineering (CiET 1819/10), Chan Zuckerberg Initiative (CZIF2022-316777), ESRF HOAHub MD-1389, Diamond Light Source beamtimes (MG29633-1 and SM29784-6). A.L.P. acknowledges support from the i4health Centre for Doctoral Training.

AUTHOR CONTRIBUTIONS

Conceptualization, A.L.P., C.M.D., H.D., N.J.T., B.K.B., A.A.P., H.S.G., and P.D.L.; methodology, A.L.P., E.N., C.M.D., A.S., H.D., and H.S.G.; software, A.L.P., E.N., and B.K.B; validation, A.L.P. and E.N.; formal analysis, A.L.P. and E.N.; investigation, A.L.P., E.N., C.M.D., A.S., H.D., and H.S.G.; resources, H.D., N.J.T., B.K.B., H.S.G., and P.D.L.; data curation, A.L.P.; writing—original draft, A.L.P., E.N., A.S., F.B., B.K.B., A.A.P., H.S.G., and P.D.L.; writing—review & editing, all authors; visualization, A.L.P., E.N., and A.S.; supervision, F.B., H.S.G., and P.D.L.; project administration: H.S.G. and P.D.L.; funding acquisition, N.J.T., B.K.B., A.A.P., H.S.G., and P.D.L.

DECLARATION OF INTERESTS

The authors declare no competing interests.

SUPPLEMENTAL INFORMATION

Supplemental information can be found online at https://doi.org/10.1016/j.celbio.2025.100151.

Received: October 28, 2024
Revised: March 6, 2025
Accepted: June 27, 2025

REFERENCES

1. Ferreira, M.L., De Luca, K., Haile, L.M., Steinmetz, J.D., Culbreth, G.T., Cross, M., Kopec, J.A., Ferreira, P.H., Blyth, F.M., and Buchbinder, R. (2023). Global, regional, and national burden of low back pain, 1990–2020, its attributable risk factors, and projections to 2050: a systematic analysis of the Global Burden of Disease Study 2021. Lancet Rheumatol. *5*, e316–e329. https://doi.org/10.1016/S2665-9913(23)00098-X.
2. Bonnevie, E.D., Gullbrand, S.E., Ashinsky, B.G., Tsinman, T.K., Elliott, D. M., Chao, P.G., Smith, H.E., and Mauck, R.L. (2019). Aberrant mechanosensing in injured intervertebral discs as a result of boundary-constraint disruption and residual-strain loss. Nat. Biomed. Eng. *3*, 998–1008. https://doi.org/10.1038/s41551-019-0458-4.
3. Aebi, M. (2005). The adult scoliosis. Eur. Spine J. *14*, 925–948. https://doi.org/10.1007/s00586-005-1053-9.
4. Desmoulin, G.T., Pradhan, V., and Milner, T.E. (2020). Mechanical Aspects of Intervertebral Disc Injury and Implications on Biomechanics. Spine *45*, E457–E464. https://doi.org/10.1097/BRS.0000000000003291.
5. Cao, Y., Liao, S., Zeng, H., Ni, S., Tintani, F., Hao, Y., Wang, L., Wu, T., Lu, H., Duan, C., et al. (2017). 3D characterization of morphological changes in the intervertebral disc and endplate during aging: A propagation phase contrast synchrotron micro-tomography study. Sci. Rep. *7*, 43094. https://doi.org/10.1038/srep43094.
6. Mente, P.L., and Lewis, J.L. (1994). Elastic modulus of calcified cartilage is an order of magnitude less than that of subchondral bone. J. Orthop. Res. *12*, 637–647. https://doi.org/10.1002/jor.1100120506.
7. Gupta, H.S., Schratter, S., Tesch, W., Roschger, P., Berzlanovich, A., Schoeberl, T., Klaushofer, K., and Fratzl, P. (2005). Two different correlations between nanoindentation modulus and mineral content in the bone–cartilage interface. J. Struct. Biol. *149*, 138–148. https://doi.org/10.1016/j.jsb.2004.10.010.
8. Das Gupta, S., Finnilä, M.A.J., Karhula, S.S., Kauppinen, S., Joukainen, A., Kröger, H., Korhonen, R.K., Thambyah, A., Rieppo, L., and Saarakkala, S. (2020). Raman microspectroscopic analysis of the tissue-specific composition of the human osteochondral junction in osteoarthritis: A pilot study. Acta Biomater. *106*, 145–155. https://doi.org/10.1016/j.actbio.2020.02.020.
9. Fratzl, P., Fratzl-Zelman, N., and Klaushofer, K. (1993). Collagen packing and mineralization. An x-ray scattering investigation of turkey leg tendon. Biophys. J. *64*, 260–266. https://doi.org/10.1016/S0006-3495(93)81362-6.
10. Törnquist, E., Isaksson, H., and Turunen, M.J. (2020). Mineralization of cortical bone during maturation and growth in rabbits. J. Bone Miner. Metab. *38*, 289–298. https://doi.org/10.1007/s00774-019-01068-y.
11. Fratzl, P., Fratzl-Zelman, N., Klaushofer, K., Vogl, G., and Koller, K. (1991). Nucleation and growth of mineral crystals in bone studied by small-angle X-ray scattering. Calcif. Tissue Int. *48*, 407–413. https://doi.org/10.1007/BF02556454.
12. Wang, Y., Azaïs, T., Robin, M., Vallée, A., Catania, C., Legriel, P., Pehau-Arnaudet, G., Babonneau, F., Giraud-Guille, M.M., and Nassif, N. (2012). The predominant role of collagen in the nucleation, growth, structure and orientation of bone apatite. Nat. Mater. *11*, 724–733. https://doi.org/10.1038/nmat3362.
13. Silva Barreto, I., Le Cann, S., Ahmed, S., Sotiriou, V., Turunen, M.J., Johansson, U., Rodriguez-Fernandez, A., Grünewald, T.A., Liebi, M., Nowlan, N.C., et al. (2020). Multiscale Characterization of Embryonic Long Bone Mineralization in Mice. Adv. Sci. (Weinh) *7*, 2002524. https://doi.org/10.1002/advs.202002524.
14. Turunen, M.J., Kaspersen, J.D., Olsson, U., Guizar-Sicairos, M., Bech, M., Schaff, F., Tägil, M., Jurvelin, J.S., and Isaksson, H. (2016). Bone mineral crystal size and organization vary across mature rat bone cortex. J. Struct. Biol. *195*, 337–344. https://doi.org/10.1016/j.jsb.2016.07.005.
15. Finnilä, M.A.J., Das Gupta, S., Turunen, M.J., Hellberg, I., Turkiewicz, A., Lutz-Bueno, V., Jonsson, E., Holler, M., Ali, N., Hughes, V., et al. (2022). Mineral Crystal Thickness in Calcified Cartilage and Subchondral Bone in Healthy and Osteoarthritic Human Knees. J. Bone Miner. Res. *37*, 1700–1710. https://doi.org/10.1002/jbmr.4642.
16. Bertinetti, L., Masic, A., Schuetz, R., Barbetta, A., Seidt, B., Wagermaier, W., and Fratzl, P. (2015). Osmotically driven tensile stress in collagen-based mineralized tissues. J. Mech. Behav. Biomed. Mater. *52*, 14–21. https://doi.org/10.1016/j.jmbbm.2015.03.010.
17. Gupta, H.S., Seto, J., Wagermaier, W., Zaslansky, P., Boesecke, P., and Fratzl, P. (2006). Cooperative deformation of mineral and collagen in bone at the nanoscale. Proc. Natl. Acad. Sci. USA *103*, 17741–17746. https://doi.org/10.1073/pnas.0604237103.
18. Zhang, Y., Lenart, B.A., Lee, J.K., Chen, D., Shi, P., Ren, J., Muehleman, C., Chen, D., and An, H.S. (2014). Histological features of endplates of the mammalian spine: From mice to men. Spine *39*, E312–E317. https://doi.org/10.1097/BRS.0000000000000174.
19. Carter, D.R., Beaupré, G.S., Giori, N.J., and Helms, J.A. (1998). Mechanobiology of skeletal regeneration. In Clin. Orthop. Relat. Res., pp. S41–S55. https://doi.org/10.1097/00003086-199810001-00006.
20. Silverman, A.A., Olszewski, J.D., Siadat, S.M., and Ruberti, J.W. (2024). Tension in the ranks: Cooperative cell contractions drive force-dependent collagen assembly in human fibroblast culture. Matter *7*, 1533–1557. https://doi.org/10.1016/j.matt.2024.01.023.
21. Wang, L., You, X., Zhang, L., Zhang, C., and Zou, W. (2022). Mechanical regulation of bone remodeling. Bone Res. *10*, 16. https://doi.org/10.1038/s41413-022-00190-4.
22. Grosland, N.M., and Goel, V.K. (2007). Vertebral endplate morphology follows bone remodeling principles. Spine *32*, E667–E673. https://doi.org/10.1097/BRS.0b013e318158cfaf.
23. Hodgkinson, T., Kelly, D.C., Curtin, C.M., and O'Brien, F.J. (2022). Mechanosignalling in cartilage: an emerging target for the treatment of osteoarthritis. Nat. Rev. Rheumatol. *18*, 67–84. https://doi.org/10.1038/s41584-021-00724-w.
24. Adams, M.A., Freeman, B.J.C., Morrison, H.P., Nelson, I.W., and Dolan, P. (2000). Mechanical Initiation of Intervertebral Disc Degeneration. Spine *25*, 1625–1636. https://doi.org/10.1097/00007632-200007010-00005.
25. Lawan, A., Crites Videman, J., and Battié, M.C. (2021). The association between vertebral endplate structural defects and back pain: a systematic review and meta-analysis. Eur. Spine J. *30*, 2531–2548. https://doi.org/10.1007/s00586-021-06865-6.
26. Hussein, A.I., and Morgan, E.F. (2013). The effect of intravertebral heterogeneity in microstructure on vertebral strength and failure patterns. Osteoporos. Int. *24*, 979–989. https://doi.org/10.1007/s00198-012-2039-1.
27. Ma, C., Du, T., Niu, X., and Fan, Y. (2022). Biomechanics and mechanobiology of the bone matrix. Bone Res. *10*, 59. https://doi.org/10.1038/s41413-022-00223-y.
28. Inamdar, S.R., Knight, D.P., Terrill, N.J., Karunaratne, A., Cacho-Nerin, F., Knight, M.M., and Gupta, H.S. (2017). The Secret Life of Collagen: Temporal Changes in Nanoscale Fibrillar Pre-Strain and Molecular Organization during Physiological Loading of Cartilage. ACS Nano *11*, 9728–9737. https://doi.org/10.1021/acsnano.7b00563.
29. Badar, W., Ali, H., Brooker, O.N., Newham, E., Snow, T., Terrill, N.J., Tozzi, G., Fratzl, P., Knight, M.M., and Gupta, H.S. (2022). Collagen pre-strain discontinuity at the bone—Cartilage interface. PLoS One *17*, e0273832. https://doi.org/10.1371/journal.pone.0273832.
30. Forien, J.B., Fleck, C., Cloetens, P., Duda, G., Fratzl, P., Zolotoyabko, E., and Zaslansky, P. (2015). Compressive Residual Strains in Mineral Nanoparticles as a Possible Origin of Enhanced Crack Resistance in Human Tooth Dentin. Nano Lett. *15*, 3729–3734. https://doi.org/10.1021/acs.nanolett.5b00143.
31. Polishchuk, I., Bracha, A.A., Bloch, L., Levy, D., Kozachkevich, S., Etinger-Geller, Y., Kauffmann, Y., Burghammer, M., Giacobbe, C., Villanova, J., et al. (2017). Coherently aligned nanoparticles within a biogenic single crystal: A biological prestressing strategy. Science *358*, 1294–1298. https://doi.org/10.1126/science.aaj2156.

32. Silveira, A., Davydok, A., Krywka, C., Scheel, M., Weitkamp, T., Fleck, C., Shahar, R., and Zaslansky, P. (2025). Nanocrystal Compressive Residual Stresses: A Strategy to Strengthen the Bony Spines of Osteocytic and Anosteocytic Fish. Adv. Sci. (Weinh) *12*, e2410617. https://doi.org/10.1002/ADVS.202410617.

33. Ping, H., Wagermaier, W., Horbelt, N., Scoppola, E., Li, C., Werner, P., Fu, Z., and Fratzl, P. (2022). Mineralization generates megapascal contractile stresses in collagen fibrils. Science *376*, 188–192. https://doi.org/10.1126/science.abm2664.

34. Bidan, C.M., Kollmannsberger, P., Gering, V., Ehrig, S., Joly, P., Petersen, A., Vogel, V., Fratzl, P., and Dunlop, J.W.C. (2016). Gradual conversion of cellular stress patterns into pre-stressed matrix architecture during in vitro tissue growth. J. R. Soc. Interface *13*, 20160136. https://doi.org/10.1098/rsif.2016.0136.

35. Dall'Ara, E., and Tozzi, G. (2022). Digital volume correlation for the characterization of musculoskeletal tissues: Current challenges and future developments. Front. Bioeng. Biotechnol. *10*, 1010056. https://doi.org/10.3389/fbioe.2022.1010056.

36. Bay, B.K., Smith, T.S., Fyhrie, D.P., and Saad, M. (1999). Digital volume correlation: Three-dimensional strain mapping using X-ray tomography. Exp. Mech. *39*, 217–226. https://doi.org/10.1007/BF02323555.

37. Bay, B.K. (2008). Methods and applications of digital volume correlation. J. Strain Anal. Eng. Des. *43*, 745–760. https://doi.org/10.1243/03093247JSA436.

38. Turunen, M.J., Le Cann, S., Tudisco, E., Lovric, G., Patera, A., Hall, S.A., and Isaksson, H. (2020). Sub-trabecular strain evolution in human trabecular bone. Sci. Rep. *10*, 13788. https://doi.org/10.1038/s41598-020-69850-x.

39. Madi, K., Staines, K.A., Bay, B.K., Javaheri, B., Geng, H., Bodey, A.J., Cartmell, S., Pitsillides, A.A., and Lee, P.D. (2020). In situ characterization of nanoscale strains in loaded whole joints via synchrotron X-ray tomography. Nat. Biomed. Eng. *4*, 343–354. https://doi.org/10.1038/s41551-019-0477-1.

40. Dejea, H., Pierantoni, M., Orozco, G.A., B Wrammerfors, E.T., Gstöhl, S.J., Schlepütz, C.M., and Isaksson, H. (2024). In Situ Loading and Time-Resolved Synchrotron-Based Phase Contrast Tomography for the Mechanical Investigation of Connective Knee Tissues: A Proof-of-Concept Study. Adv. Sci. (Weinh) *11*, e2308811. https://doi.org/10.1002/advs.202308811.

41. Disney, C.M., Mo, J., Eckersley, A., Bodey, A.J., Hoyland, J.A., Sherratt, M.J., Pitsillides, A.A., Lee, P.D., and Bay, B.K. (2022). Regional variations in discrete collagen fibre mechanics within intact intervertebral disc resolved using synchrotron computed tomography and digital volume correlation. Acta Biomater. *138*, 361–374. https://doi.org/10.1016/j.actbio.2021.10.012.

42. Tavana, S., Masouros, S.D., Baxan, N., Freedman, B.A., Hansen, U.N., and Newell, N. (2020). The Effect of Degeneration on Internal Strains and the Mechanism of Failure in Human Intervertebral Discs Analyzed Using Digital Volume Correlation (DVC) and Ultra-High Field MRI. Front. Bioeng. Biotechnol. *8*, 610907. https://doi.org/10.3389/fbioe.2020.610907.

43. Palanca, M., Cavazzoni, G., and Dall'Ara, E. (2023). The role of bone metastases on the mechanical competence of human vertebrae. Bone *173*, 116814. https://doi.org/10.1016/j.bone.2023.116814.

44. Zimmermann, E.A., Schaible, E., Bale, H., Barth, H.D., Tang, S.Y., Reichert, P., Busse, B., Alliston, T., Ager, J.W., and Ritchie, R.O. (2011). Age-related changes in the plasticity and toughness of human cortical bone at multiple length scales. Proc. Natl. Acad. Sci. USA *108*, 14416–14421. https://doi.org/10.1073/pnas.1107966108.

45. Grünewald, T.A., Liebi, M., Wittig, N.K., Johannes, A., Sikjaer, T., Rejnmark, L., Gao, Z., Rosenthal, M., Guizar-Sicairos, M., Birkedal, H., et al. (2020). Mapping the 3D orientation of nanocrystals and nanostructures in human bone: Indications of novel structural features. Sci. Adv. *6*, eaba4171. https://doi.org/10.1126/sciadv.aba4171.

46. Xavier, F., Jauregui, J.J., Cornish, N., Jason-Rousseau, R., Chatterjee, D., Feuer, G., Hayes, W., Kapadia, B.H., Carter, J.N., Yoshihara, H., et al. (2017). Regional Variations in Shear Strength and Density of the Human Thoracic Vertebral Endplate and Trabecular Bone. Int. J. Spine Surg. Aurora *11*, 7. https://doi.org/10.14444/4007.

47. Patel, R.R., Noshchenko, A., Dana Carpenter, R.D., Baldini, T., Frick, C.P., Patel, V.V., and Yakacki, C.M. (2018). Evaluation and Prediction of Human Lumbar Vertebrae Endplate Mechanical Properties Using Indentation and Computed Tomography. J. Biomech. Eng. *140*, 1010111–1010119. https://doi.org/10.1115/1.4040252.

48. Wu, Y., Loaiza, J., Banerji, R., Blouin, O., and Morgan, E. (2021). Structure-function relationships of the human vertebral endplate. JOR Spine *4*, e1170. https://doi.org/10.1002/jsp2.1170.

49. Hulme, P.A., Ferguson, S.J., and Boyd, S.K. (2008). Determination of vertebral endplate deformation under load using micro-computed tomography. J. Biomech. *41*, 78–85. https://doi.org/10.1016/j.jbiomech.2007.07.018.

50. Zehra, U., Robson-Brown, K., Adams, M.A., and Dolan, P. (2015). Porosity and thickness of the vertebral endplate depend on local mechanical loading. Spine *40*, 1173–1180. https://doi.org/10.1097/BRS.0000000000000925.

51. Curry, W.H., Pintar, F.A., Doan, N.B., Nguyen, H.S., Eckardt, G., Baisden, J.L., Maiman, D.J., Paskoff, G.R., Shender, B.S., and Stemper, B.D. (2016). Lumbar spine endplate fractures: Biomechanical evaluation and clinical considerations through experimental induction of injury. J. Orthop. Res. *34*, 1084–1091. https://doi.org/10.1002/JOR.23112.

52. McKay, M.L., Jackman, T.M., Hussein, A.I., Guermazi, A., Liu, J., and Morgan, E.F. (2020). Association of vertebral endplate microstructure with bone strength in men and women. Bone *131*, 115147. https://doi.org/10.1016/J.BONE.2019.115147.

53. Reinhard, C., Drakopoulos, M., Ahmed, S.I., Deyhle, H., James, A., Charlesworth, C.M., Burt, M., Sutter, J., Alexander, S., Garland, P., et al. (2021). Beamline K11 DIAD: a new instrument for dual imaging and diffraction at Diamond Light Source. J. Synchrotron Radiat. *28*, 1985–1995. https://doi.org/10.1107/S1600577521009875.

54. Disney, C.M., Vo, N.T., Bodey, A.J., Bay, B.K., and Lee, P.D. (2023). Image quality and scan time optimisation for in situ phase contrast x-ray tomography of the intervertebral disc. J. Mech. Behav. Biomed. Mater. *138*, 105579. https://doi.org/10.1016/j.jmbbm.2022.105579.

55. Disney, C.M., Eckersley, A., McConnell, J.C., Geng, H., Bodey, A.J., Hoyland, J.A., Lee, P.D., Sherratt, M.J., and Bay, B.K. (2019). Synchrotron tomography of intervertebral disc deformation quantified by digital volume correlation reveals microstructural influence on strain patterns. Acta Biomater. *92*, 290–304. https://doi.org/10.1016/J.ACTBIO.2019.05.021.

56. Newell, N., Little, J.P., Christou, A., Adams, M.A., Adam, C.J., and Masouros, S.D. (2017). Biomechanics of the human intervertebral disc: A review of testing techniques and results. J. Mech. Behav. Biomed. Mater. *69*, 420–434. https://doi.org/10.1016/j.jmbbm.2017.01.037.

57. Bakdash, J.Z., and Marusich, L.R. (2017). Repeated measures correlation. Front. Psychol. *8*, 456. https://doi.org/10.3389/fpsyg.2017.00456.

58. Holm, S. (1979). A simple sequential rejective method procedure. Scand. J. Stat. *6*.

59. Wittig, N.K., Bach-Gansmo, F.L., Birkbak, M.E., Laugesen, M., Brüel, A., Thomsen, J.S., and Birkedal, H. (2016). Organ and tissue level properties are more sensitive to age than osteocyte lacunar characteristics in rat cortical bone. Bone Rep. *4*, 28–34. https://doi.org/10.1016/j.bonr.2015.11.003.

60. Evans, L.A.E., and Pitsillides, A.A. (2022). Structural clues to articular calcified cartilage function: A descriptive review of this crucial interface tissue. J. Anat. *241*, 875–895. https://doi.org/10.1111/joa.13728.

61. Currey, J. (2004). Incompatible mechanical properties in compact bone. J. Theor. Biol. *231*, 569–580. https://doi.org/10.1016/j.jtbi.2004.07.013.

62. Zizak, I., Roschger, P., Paris, O., Misof, B.M., Berzlanovich, A., Bernstorff, S., Amenitsch, H., Klaushofer, K., and Fratzl, P. (2003). Characteristics of mineral particles in the human bone/cartilage interface. J. Struct. Biol. *141*, 208–217. https://doi.org/10.1016/S1047-8477(02)00635-4.

63. Rahman, T., Tavana, S., Baxan, N., Raftery, K.A., Morgan, G., Schaer, T. P., Smith, N., Moore, A., Bull, J., Stevens, M.M., et al. (2023). Quantifying internal intervertebral disc strains to assess nucleus replacement device designs: a digital volume correlation and ultra-high-resolution MRI study. Front. Bioeng. Biotechnol. *11*, 1229388. https://doi.org/10.3389/fbioe.2023.1229388.

64. Lamoureux, F., Baud'huin, M., Duplomb, L., Heymann, D., and Rédini, F. (2007). Proteoglycans: Key partners in bone cell biology. BioEssays *29*, 758–771. https://doi.org/10.1002/bies.20612.

65. Poole, A.R., Kojima, T., Yasuda, T., Mwale, F., Kobayashi, M., and Laverty, S. (2001). Composition and structure of articular cartilage: A template for tissue repair. Clin. Orthop. Relat. Res. *391*, S26–S33. https://doi.org/10.1097/00003086-200110001-00004.

66. Reznikov, N., Bilton, M., Lari, L., Stevens, M.M., and Kröger, R. (2018). Fractal-like hierarchical organization of bone begins at the nanoscale. Science *360*, eaao2189. https://doi.org/10.1126/science.aao2189.

67. Kumbolder, V., Morin, C., Scheiner, S., and Hellmich, C. (2024). Hierarchical elastoplasticity of cortical bone: Observations, mathematical modeling, validation. Mech. Mater. *198*, 105140. https://doi.org/10.1016/J.MECHMAT.2024.105140.

68. Anderson, H.C. (1995). Molecular biology of matrix vesicles. Clin. Orthop. Relat. Res. *314*, 266–280. https://doi.org/10.1097/00003086-199505000-00034.

69. Alijani, H., and Vaughan, T.J. (2024). Exploring the hierarchical structure of lamellar bone and its impact on fracture behaviour: A computational study using a phase field damage model. J. Mech. Behav. Biomed. Mater. *153*, 106471. https://doi.org/10.1016/j.jmbbm.2024.106471.

70. Jäger, I., and Fratzl, P. (2000). Mineralized collagen fibrils: A mechanical model with a staggered arrangement of mineral particles. Biophys. J. *79*, 1737–1746. https://doi.org/10.1016/S0006-3495(00)76426-5.

71. Zehra, U., Tryfonidou, M., Iatridis, J.C., Illien-Jünger, S., Mwale, F., and Samartzis, D. (2022). Mechanisms and clinical implications of intervertebral disc calcification. Nat. Rev. Rheumatol. *18*, 352–362. https://doi.org/10.1038/s41584-022-00783-7.

72. Peng, Y., Zhuang, Y., Liu, Y., Le, H., Li, D., Zhang, M., Liu, K., Zhang, Y., Zuo, J., and Ding, J. (2023). Bioinspired gradient scaffolds for osteochondral tissue engineering. Exploration (Beijing) *3*, 20210043. https://doi.org/10.1002/EXP.20210043.

73. Kumar, A., Kargozar, S., Baino, F., and Han, S.S. (2019). Additive Manufacturing Methods for Producing Hydroxyapatite and Hydroxyapatite-Based Composite Scaffolds: A Review. Front. Mater. *6*. https://doi.org/10.3389/fmats.2019.00313.

74. Kumar, S., Nehra, M., Kedia, D., Dilbaghi, N., Tankeshwar, K., and Kim, K. H. (2020). Nanotechnology-based biomaterials for orthopaedic applications: Recent advances and future prospects. Mater. Sci. Eng. C Mater. Biol. Appl. *106*, 110154. https://doi.org/10.1016/j.msec.2019.110154.

75. O'Connell, G.D., Vresilovic, E.J., and Elliott, D.M. (2007). Comparison of Animals Used in Disc Research to Human Lumbar Disc Geometry. Spine *32*, 328–333. https://doi.org/10.1097/01.brs.0000253961.40910.c1.

76. Peña Fernández, M., Cipiccia, S., Dall'Ara, E., Bodey, A.J., Parwani, R., Pani, M., Blunn, G.W., Barber, A.H., and Tozzi, G. (2018). Effect of SR-microCT radiation on the mechanical integrity of trabecular bone using in situ mechanical testing and digital volume correlation. J. Mech. Behav. Biomed. Mater. *88*, 109–119. https://doi.org/10.1016/J.JMBBM.2018.08.012.

77. Barth, H.D., Zimmermann, E.A., Schaible, E., Tang, S.Y., Alliston, T., and Ritchie, R.O. (2011). Characterization of the effects of x-ray irradiation on the hierarchical structure and mechanical properties of human cortical bone. Biomaterials *32*, 8892–8904. https://doi.org/10.1016/j.biomaterials.2011.08.013.

78. Parmenter, A., Newham, E., Sharma, A., Disney, C., Deyhle, H., Bosi, F., Terrill, N., Bay, B., Pitsillides, A., Gupta, H., et al. (2024) Supplemental Data: Variations in mineral prestrain, nanostructure, and microarchitecture play a role in intervertebral disc loading. https://doi.org/10.5522/04/26789212.

79. Rau, C., Wagner, U., Pešić, Z., and De Fanis, A. (2011). Coherent imaging at the Diamond beamline I13. Physica Status Solidi (a) *208*, 2522–2525. https://doi.org/10.1002/PSSA.201184272.

80. Atwood, R.C., Bodey, A.J., Price, S.W.T., Basham, M., and Drakopoulos, M. (2015). A high-throughput system for high-quality tomographic reconstruction of large datasets at diamond light source. Philos. Trans. A Math. Phys. Eng. Sci. *373*, 20140398. https://doi.org/10.1098/rsta.2014.0398.

81. Vo, N.T., Atwood, R.C., and Drakopoulos, M. (2015). Radial lens distortion correction with sub-pixel accuracy for X-ray micro-tomography. Opt. Express *23*, 32859–32868. https://doi.org/10.1364/OE.23.032859.

82. Vo, N.T., Atwood, R.C., and Drakopoulos, M. (2018). Superior techniques for eliminating ring artifacts in X-ray micro-tomography. Opt. Express *26*, 28396–28412. https://doi.org/10.1364/OE.26.028396.

83. van Aarle, W., Palenstijn, W.J., Cant, J., Janssens, E., Bleichrodt, F., Dabravolski, A., De Beenhouwer, J., Joost Batenburg, K., and Sijbers, J. (2016). Fast and flexible X-ray tomography using the ASTRA toolbox. Opt. Express *24*, 25129–25147. https://doi.org/10.1364/OE.24.025129.

84. Paganin, D., Mayo, S.C., Gureyev, T.E., Miller, P.R., and Wilkins, S.W. (2002). Simultaneous phase and amplitude extraction from a single defocused image of a homogeneous object. J. Microsc. *206*, 33–40. https://doi.org/10.1046/j.1365-2818.2002.01010.x.

85. Schindelin, J., Arganda-Carreras, I., Frise, E., Kaynig, V., Longair, M., Pietzsch, T., Preibisch, S., Rueden, C., Saalfeld, S., Schmid, B., et al. (2012). Fiji: An open-source platform for biological-image analysis. Nat. Methods *9*, 676–682. https://doi.org/10.1038/nmeth.2019.

86. Vo, N.T., Atwood, R.C., Drakopoulos, M., and Connolley, T. (2021). Data processing methods and data acquisition for samples larger than the field of view in parallel-beam tomography. Opt. Express *29*, 17849–17874. https://doi.org/10.1364/OE.418448.

87. Liu, L., and Morgan, E.F. (2007). Accuracy and precision of digital volume correlation in quantifying displacements and strains in trabecular bone. J. Biomech. *40*, 3516–3520. https://doi.org/10.1016/j.jbiomech.2007.04.019.

88. Besnard, C., Marie, A., Sasidharan, S., Deyhle, H., James, A.M., Ahmed, S.I., Reinhard, C., Harper, R.A., Shelton, R.M., Landini, G., et al. (2024). The DIAD Approach to Correlative Synchrotron X-ray Imaging and Diffraction Analysis of Human Enamel. Chem. Biomed. Imaging *2*, 222–232. https://doi.org/10.1021/cbmi.3c00122.

89. Basham, M., Filik, J., Wharmby, M.T., Chang, P.C.Y., El Kassaby, B., Gerring, M., Aishima, J., Levik, K., Pulford, B.C.A., Sikharulidze, I., et al. (2015). Data Analysis WorkbeNch (DAWN). J. Synchrotron Radiat. *22*, 853–858. https://doi.org/10.1107/S1600577515002283.

90. Newville, M., Ingargiola, A., Stensitzki, T., and Allen, D.B. (2014). LMFIT: Non-Linear Least-Square Minimization and Curve-Fitting for Python. Zenodo. https://doi.org/10.5281/zenodo.598352.

91. Lange, C., Li, C., Manjubala, I., Wagermaier, W., Kühnisch, J., Kolanczyk, M., Mundlos, S., Knaus, P., and Fratzl, P. (2011). Fetal and postnatal mouse bone tissue contains more calcium than is present in hydroxyapatite. J. Struct. Biol. *176*, 159–167. https://doi.org/10.1016/j.jsb.2011.08.003.

92. Domander, R., Felder, A.A., and Doube, M. (2021). BoneJ2 - refactoring established research software. Wellcome Open Res. *6*, 37. https://doi.org/10.12688/wellcomeopenres.16619.2.

93. Dougherty, R., and Kunzelmann, K.-H. (2007). Computing Local Thickness of 3D Structures with ImageJ. Microsc. Microanal. *13*. https://doi.org/10.1017/S1431927607074430.

94. Hildebrand, T., and Rüegsegger, P. (1997). A new method for the model-independent assessment of thickness in three-dimensional images. J. Microsc. *185*, 67–75. https://doi.org/10.1046/j.1365-2818.1997.1340694.x.

95. Harrigan, T.P., and Mann, R.W. (1984). Characterization of microstructural anisotropy in orthotropic materials using a second rank tensor. J. Mater. Sci. *19*, 761–767. https://doi.org/10.1007/BF00540446.

96. Odgaard, A. (1997). Three-dimensional methods for quantification of cancellous bone architecture. Bone *20*, 315–328. https://doi.org/10.1016/S8756-3282(97)00007-0.

97. Toriwaki, J., and Yonekura, T. (2002). Euler Number and Connectivity Indexes of a Three Dimensional Digital Picture. Forma *17*, 183–209.

98. Odgaard, A., and Gundersen, H.J.G. (1993). Quantification of connectivity in cancellous bone, with special emphasis on 3-D reconstructions. Bone *14*, 173–182. https://doi.org/10.1016/8756-3282(93)90245-6.

99. Marusich, L.R., and Bakdash, J.Z. (2021). rmcorrShiny: A web and standalone application for repeated measures correlation. F1000Res *10*, 697. https://doi.org/10.12688/f1000research.55027.2.